Journal of MATERIALS RESEARCH

Invited Feature Review
DOI:10.1557/s43578-023-01271-8

EARLY CAREER SCHOLARS IN MATERIALS SCIENCE

ANNUAL ISSUE

Metal powder as feedstock for laser-based additive manufacturing: From production to powder modification

Laura E. T. Mathias[1], Vitor E. Pinotti[1], Bruna F. Batistão[1], Nicolas Rojas-Arias[1], Gustavo Figueira[1], Angelo F. Andreoli[2,a], Piter Gargarella[1,2,3]

[1] Graduate Program in Materials Science and Engineering, Federal University of São Carlos, Rodovia Washington Luís, km 235 SP-310, São Carlos, SP 13565-905, Brazil
[2] Department of Materials Engineering, Federal University of São Carlos, Rodovia Washington Luís, km 235 SP-310, São Carlos, SP 13565-905, Brazil
[3] Center of Characterization and Development of Materials, Federal University of São Carlos, Rodovia Washington Luís, km 235 SP-310, São Carlos, SP 13565-905, Brazil
[a] Address all correspondence to this author. e-mail: angelo.andreoli@ufscar.br

Received: 2 June 2023; accepted: 11 December 2023; published online: 29 December 2023

Laser powder bed fusion (L-PBF) and direct laser deposition (DLD) are the two main processes currently used in the additive manufacturing (AM) of metals. For both methods, metal powders are used as feedstock, and they must present specific physical and chemical properties to ensure optimal processing and reliable and reproducible printing results. Particle morphology, size distribution, and flowability, among other factors, depend on the powder production process and directly influence the processing parameters and physical characteristics of the parts built by AM. This systematic review presents different concepts involving L-PBF and DLD manufacturing and the application of metal powders. The methods used to produce and characterize metal powders and the modification techniques to improve their processability by AM are detailed and discussed. Environmental and health risks are also presented, and safety measures that must be considered while handling metal powders. Some key topics requiring attention for further development are highlighted.

Angelo F. Andreoli

Angelo F. Andreoli has received his Ph.D. from the Technische Universität Dresden, Germany, in 2022. He is currently a Postdoctoral fellow at the Federal University of São Carlos, Brazil. He is involved with research in the fields of gas atomization and additive manufacturing. His main research interests are phase transformations, microstructural evolution, and in situ X-ray diffraction investigations of phase transformations in metallic alloys. Previously, he spent four years working with the non-equilibrium solidification of metals at the IFW Dresden. He was awarded the Ehrenfried Walther von Tschirnhaus-Plakette prize des IFW Dresden, for graduating with the highest distinction Summa cum Laude. During his master's degree at the University of São Paulo (USP/EESC), Brazil, he was involved with research in resistance welding of bulk metallic glasses. He is graduated from the São Paulo State Technological College (FATEC) Brazil, in 2015, with a degree in Mechanical Technology—Welding Processes.

Introduction

Additive manufacturing (AM) is a category of processes that manufactures parts by adding materials layer by layer, producing the part from a bottom-up perspective in opposition to subtractive manufacturing methodologies, which have a top-down approach [1]. Additive manufacturing enables design flexibility, reduces the amount of energy and feedstock required, and can reduce the lead time and production costs of small batches due to the high added value and the possibility of manufacturing complex parts in addition to a higher degree of automation

associated with the possibility of controlling the process remotely [2]. It is mainly applied in rapid prototyping to reduce the overall time-to-market of new components. Recently, this technology has been used to produce components with complex structural shapes that are challenging or impossible to manufacture by conventional fabrication routes, such as casting or subtractive manufacturing [3]. The main applications of AM are in the aerospace, automotive, biomedical (including dental and orthopedics), oil and gas (fuel nozzles, valves, etc.), housing, and tooling industries [2].

A successful combination of feedstock characteristics and energy delivery is required to achieve effective material joining, and these combinations differ according to the material, process, and AM machine used [4]. It is well established that feedstock quality is the key to process performance and final part quality. Unlike other types of feedstocks such as wires and sheets, the small size of metallic powders implies an unpaired set of good surface finish, high density, and ability to produce intricate parts [1]. Regardless of the powder delivery method, which changes from powder spreading in laser powder bed fusion (L-PBF) to coaxial feeding in direct energy deposition (DED) [1], the interaction between powder, power source, and the previously consolidated layers is extremely complex. The root of defects such as pores, denudation, and splatters is deeply correlated to the melt pool dynamics, including recoil pressure and the Marangoni effect [5]. The discrete nature of the metallic powder also influences the mass and heat transfer through the powder bed and the solidified layers [5].

The powder characteristics influence the bulk material properties of built parts, such as density and porosity [6]. Some introductory statements related to powder particle size are that broader particle size distributions (PSD) generate higher powder bulk density, while narrower PSD flows better. Smaller mean particle size requires lower energy density and enables better surface finish, and combined with narrower PSD, avoids segregation generating parts with improved strength and hardness [7]. Particle morphology is also essential, as more spherical particles with smoother surfaces have improved flowability and, thus, result in a more uniform powder bed. The effect of the atomizing medium, in addition to influencing the average size and PSD, can also slightly modify the alloy's chemistry, affecting the final part properties [8]. Furthermore, powder costs are among the most significant costs associated with AM [7]. The feedstock used is critical to ensure good processability and quality of the final products.

It is challenging to understand the characteristics of the powder and their relationship with the AM process, as there is not a single set of powder features for all AM technologies. Flowability, for instance, depends on the type of powder deposition, the spreading system itself, and consequently, the test method [7]. In addition, no available literature addresses the main powder characteristics, from the influence of the manufacturing route to the possibility of powder modification for applications in specific processes.

This systematic review overviews the main powder characteristics and analysis techniques. It also addresses the main powder production routes, covers the critical studies on the influence of powder in L-PBF and DED processing, and compiles the focal data related to steel and aluminum alloys. Finally, aspects of powder modification to improve the performance of AM processes and the main safety issues in metal powders are discussed. Some key topics requiring attention for further development will be highlighted and discussed.

Brief overview of additive manufacturing processes

Additive manufacturing processes are classified into seven categories according to the ISO/ASTM 52900 standard, from which five are applicable to manufacture metallic parts, as shown in Fig. S1 in the Supplementary Material. Those five AM processes can be subdivided into single-step and multistep processes. The latter produces a component in a "green" state, and intermediary processes are applied to produce the final part. Multistep processes usually involve metallic particles, often in powder form, dispersed into a polymeric binding agent; therefore, the intermediary processes correspond to the debinding and sequential sintering of the green component. On the other hand, single-step processes transform the feedstock material into the final component directly, without intermediary processes. Notably, the component may require post-processing to meet the desired specification, but those AM processes are still considered single-step processes because they do not necessarily require further processing. The discussion raised in this article orbits around the powder-fed single-step processes, namely Powder Bed Fusion (PBF) and Directed Energy Deposition (DED).

Both PBF and DED can be further classified according to the energy source: laser, electron beam, or plasma/electric arc, as shown in Fig. S2 in the Supplementary Material. Each process variant can be renamed according to the power source, such as electron beam melting (EBM) for the PBF process powered by electron beam, wire-laser additive manufacturing (WLAM), wire-arc additive manufacturing (WAAM), and electron beam additive manufacturing (EBAM) for the wire-fed DED processes powered by laser, plasma/electric arc, and electron beam, respectively.

With laser-based processes, equivalent terms are used interchangeably in the literature. The term "selective laser melting" (SLM) was initially used to designate the laser-based PBF process. In 2013, SLM Solutions Group AG, Germany, deposited a patent for the term "SLM," which led to adopting new terms

to avoid copyright issues, such as direct metal laser sintering (DMLS) and L-PBF. The latter term was adopted by most of the scientific community, leading to a shift in the terminology from SLM to L-PBF. On the other hand, the laser-based DED process is often designated by laser engineering net shape (LENS), a term also protected by patent. Laser deposition welding (LDW) is also a commercial term, although it is less common. Hence, the scientific community often refers to it simply as DED or direct laser deposition (DLD).

This review article will focus on laser-based processes, the most common power source for AM of metallic components [4]. Despite being able to find valid information and correct data using any of the previously presented terms, we will adopt the terminology of L-PBF and DLD for the laser-based PBF and DED processes, respectively.

Powder characterization

The main characteristics related to the powders used in AM are presented in this section. The powders can be characterized following the ASTM F3049-14 *Standard Guide for Characterizing Properties of Metal Powders Used for Additive Manufacturing Processes*. The standard provides powder characterization information, such as determining particle size distribution, morphology, chemical composition, flow, and density.

Particle size distribution

Different methods can be applied to determine the PSD. The most important are sieving, laser diffraction analysis, and image analysis. The methods are detailed in the following.

Sieving

It consists of sieving the powder through stacked sieves with decreasing mesh sizes. According to the ASTM B214 standard, the sieve mesh opening ranges from 45 to 1000 μm. Separating powders down to the particle size of 5 μm is possible. However, such sieves are challenging to use and maintain in good condition because they are fragile and have low load capacities. Thus, the most common is to separate powders down to the particle size of 20 μm. The advantage of this technique is its low cost, while the disadvantage is its inaccuracy in separating particles < 20 μm [6]. Sieving enables separation into different particle size ranges and plotting a PSD curve based on the mass of the powder weighted from the screened fractions. However, a small amount of powder is used in each sieving step, leading to a low productivity rate. Also, as the particles get smaller they tend to agglomerate and the sieve mesh can become clogged, blocking the passage of the smaller particles [6]. This requires constant cleaning to ensure reasonable accuracy, prolonging the sieving time. Another aspect related to smaller particles is their adherence to the surface of larger particles. It occurs due to the attracting van der Waals forces and can bias the analysis results because of the difficulty separating these particles [6].

Laser diffraction analysis

The laser diffraction technique is based on light scattering phenomena. It is a technique that quickly determines a particle's geometrical dimensions by analyzing the diffraction patterns of a laser beam as it passes through objects with sizes ranging from nanometers to millimeters. The analyzed size range is 0.4–2000 μm. Analysis speed and repeatability are the main advantages of the technique. However, its accuracy is limited to spherical particles. Laser diffraction yields a PSD curve based on volume frequency, which is the most commonly used in AM reports, as exemplified in Fig. 1. One disadvantage comes from the need to know the refractive index of the material and select the best solution for the dispersion of particles. An inappropriate solution can lead to the formation of agglomerates and allow accelerated sedimentation of larger particles, giving an inaccurate result.

Image analysis

Particle size distribution measurements can also be performed by image analysis obtained by optical (OM) and scanning electron (SEM) microscopy. However, these are non-standardized methods, and the images must be post-processed to obtain their equivalent diameters based on their two-dimensional projected area, thus, PSD curves are on a number basis. The method is widely accepted in the AM industry, as it provides the most versatile approach to particle diameter, but it is essential to highlight that the technique is not very accurate [6]. Additionally, it is possible to do qualitative and quantitative analysis using image analysis, which gives information about the morphology and surface roughness.

After obtaining the representative PSD curve it is necessary to analyze it. Various PSD curves exist: normal, log-normal, and multimodal, to name a few, and atomized metal powders typically exhibit a log-normal PSD [6]. Two characteristics are required to describe the PSD: mean particle size (D_m) and deviation. The most common way to estimate the distribution spread is using the geometric standard deviation (σ_g). The σ_g is obtained by dividing the 50 % value by the 84 % value on the same percentage of the cumulative curve [6]. Also, other important parameters can be extracted from the PSD curve; values of the diameters corresponding to 10 % (D_{10}), 50 % (D_{50}), and 90 % (D_{90}) of the cumulative curve. Therefore, the PSD is necessary for a complete characterization instead of the average, maximum, or minimum values of the size range [10].

New techniques have been developed to determine PSD. Dynamic image analysis (DIA) is a non-invasive technology based on an automatic video system that captures and analyzes images of a metal powder. The captured images are counted and grouped according to their dimensions and shape parameters, forming a database. An example of these parameters is shown in Fig. 2. Dynamic image analysis is more precise, easier to use, and requires a shorter time to analyze different samples than traditional methods [11].

As previously described, each method used to determine PSD has its particular methodology for collecting and representing the data. It is possible to convert one data type into another

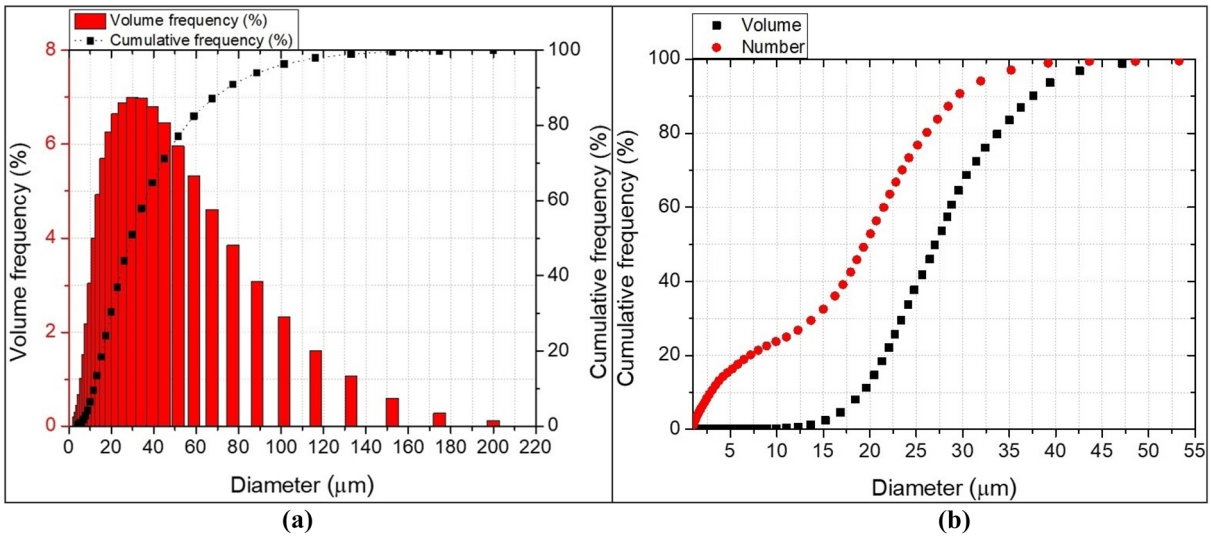

Figure 1: (a) Particle size distribution of gas-atomized AISI A2 tool steel powder. *Reproduced with permission from Ref.* [9]; (b) illustration of different particle size distributions considering both number and volume distribution.

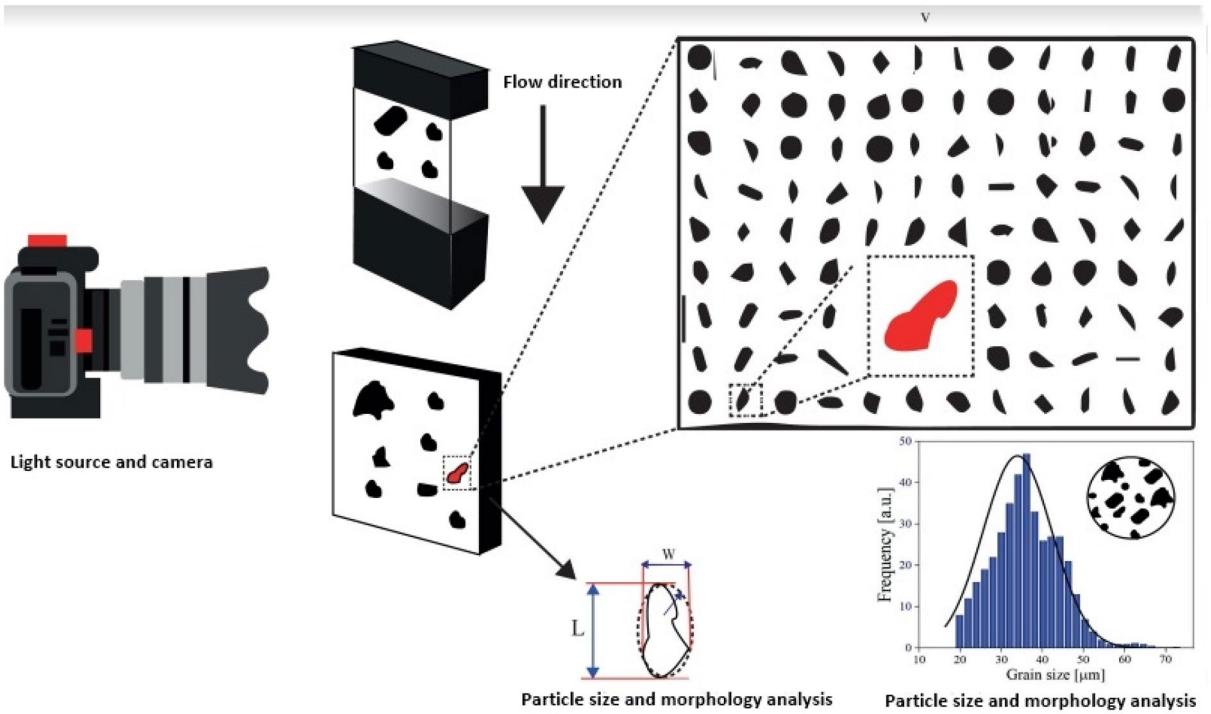

Figure 2: Schematics of the dynamic image analysis (DIA) method. Imaging of metallic particle samples; analysis using a database until determining the type of morphology for each particle measured; determining the mean radius and construction of a size distribution histogram.

through assumptions about particle shape and properties. For example, Fig. 1(b) shows microscopy data of a 304L stainless steel powder whose distribution was initially represented in number and transformed into volume [6]. Analysis of Fig. 1(b) depicts drastic differences between the curves. While the number distribution shows many particles < 15 µm, the volume distribution describes only a small number of fine powders. Since the volume of each particle is proportional to the diameter to the power of three, small particles correspond to only a minute fraction of the total volume occupied by the powder in a given sample. Thus, volumetric distributions can be misleading when the presence of small particles is of particular interest. It is vital to analyze the PSD considering the number of particles and their volumetric distribution [6].

Morphology

Morphology analysis comprehends factors and parameters that describe particle size, shape, and surface roughness. The powder shape is determined by the dimensions of the particle and its contour surface [6]. Figure 3(a) shows gas-atomized particles of AlCoCrFeNi high-entropy alloy analyzed by SEM images. It is possible to identify both spherical and non-spherical particles [12].

Chu et al. [13] highlighted two other factors that influence the processability of powder in L-PBF: satellite particles and agglomerates. Satellite particles are small particles attached to the surface of large ones and, consequently, change the particle shape factor (reduce sphericity), leading to non-uniform packing and/or feeding [examples are indicated by blue arrows in Figure 3(b)]. On the other hand, agglomerates of small particles occur due to cohesion forces and, consequently, large powder clusters are formed, which are irregular and also disturb the packing and feeding of feedstock [yellow circles in Fig. 3(c)] [13].

Describing the morphology of particles qualitatively and quantitatively can be challenging, especially if the particles are irregular and do not resemble primitive shapes. The qualitative description of powder particles follows the ASTM B243-13 standard, which describes the general shape of powder particles. Several researchers have approached the problem by formulating equations that yield dimensionless ratios (shape factors) [14]. Circularity (Eq. 1) and aspect ratio (Eq. 2) are, by far, the most commonly used shape factors in powders applied in AM [6].

$$\text{Circularity} = \frac{4 * \pi * A}{p^2}, \tag{1}$$

where 'A' is the projected area of the particle and 'P' represents the particle perimeter.

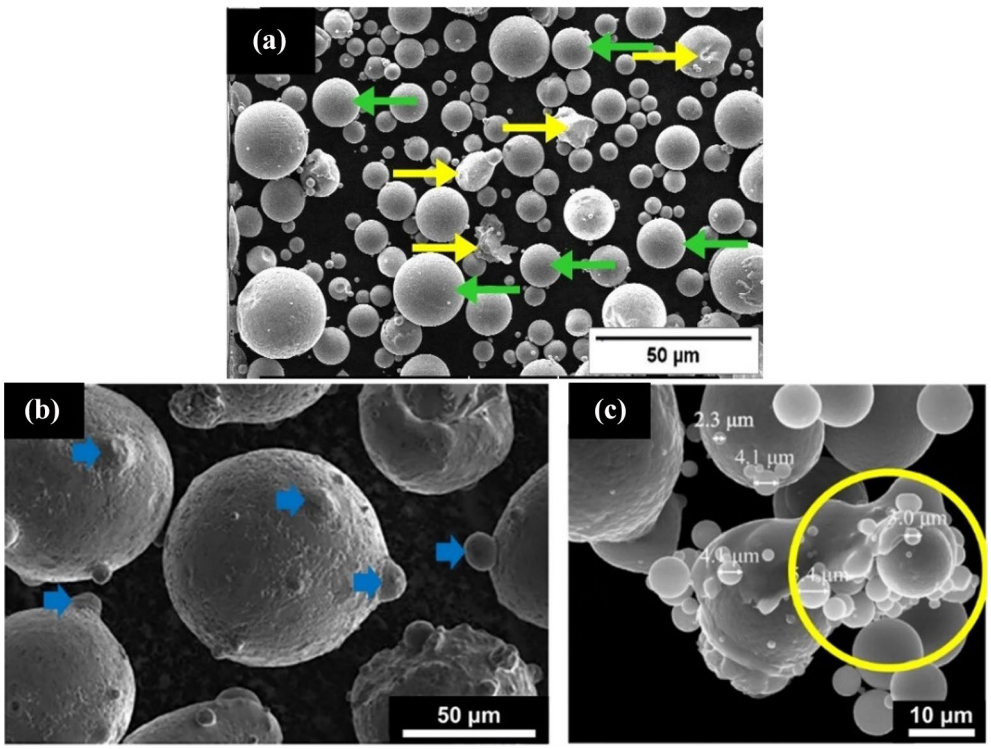

Figure 3: (a) SEM image of AlCoCrFeNi high-entropy alloy particles obtained by gas atomization (green arrows indicate examples of spherical particles, while yellow ones show non-spherical morphologies). *Reproduced under the terms of the Creative Commons CC-BY license* [12]. SEM images identifying: (b) satellite particles in gas-atomized particles; (c) powder cluster formed due to agglomeration of small gas-atomized particles. *Reproduced under the terms of the Creative Commons CC-BY-NC-ND license* [13].

$$\text{Aspect ratio} = \frac{l}{L} \quad (2)$$

where 'l' represents the minor axis length perpendicular to the major axis and 'L' corresponds to the major axis length connecting the two most distant points on the projection area A.

The particle surface topography is also essential, and the roughness degree influences the frictional forces between particles [6]. Particle surface profile can be round and smooth or present irregularities. The topography can be obtained by conducting an SEM image analysis of the surface particle.

Flowability

Flowability is the ability of a powder to flow, and it is a function of interparticle friction. Particle flow decreases with increasing interparticle friction. The powder properties (PSD and morphology) and the interaction between particles are the major factors determining powder flow. Flowability is highly dependent on the properties of the particles, and it is also a function of their interactions with the environment (e.g., temperature, and humidity) [7]. The balance between the forces that generate particle movement (gravity and applied external forces) and those that prevent it (frictional forces, outer surfaces, and forces between neighboring particles) characterize the flow behavior. These forces include mechanical friction, mechanical interlocking, van der Waals, capillary, electrostatic, and magnetic forces, and they are determined by the combination of powder particle size and PSD, particle shape, material density, particle roughness, surface chemistry, oxidation, and water content [15].

Flowability is not intrinsic because it relates to the equipment and test conditions. Thus, flowability cannot be characterized by a single technique because it is a complex phenomenon. One method is the Hausner ratio (HR) (Eq. 3):

$$\text{HR} = \frac{\rho_t}{\rho_a}, \quad (3)$$

where 'ρ_t' is the tapped bulk density of a powder and 'ρ_a' is the aerated bulk density. This ratio can also indicate powder flowability, where HR < 1.25 is often related to free-flowing powders, while powders with HR > 1.40 are considered cohesive and non-flowing [16]. Another indicator of flowability, calculated from the powder density, is Carr's compressibility index (CI) (Eq. 4), defined as

$$\text{CI} = \frac{\rho_t - \rho_a}{\rho_t}. \quad (4)$$

Although the indicators mentioned above are reportedly used to describe powder flowability, they are unsuitable for AM applications. Both indicators require tapped density as a parameter, which means they must be used under steady conditions. The dynamic powder handling during AM disqualifies using the HR and CI as suitable indicators of powder flowability for AM and any other process involving dynamic powder handling [16].

The widely used and standardized methods are the Hall flowmeter/funnel and the Carney funnel. The two methods are the only ones mentioned in the ASTM F3049 standard. These tests are based on the principle of the critical angle of repose, which states that a powder with high flowability requires a smaller slope to start flowing. Flowability is measured by inserting a known mass of powder into the funnel, and then the time needed to empty the funnel by permitting the powder to fall freely is considered the flowability indicator. The funnel tests are simple comparative tests that can provide precise results about the behavior of a powder during its processing [7].

While the Hall and Carney funnels are based on the angle of repose principle, other techniques are based on different physical principles, such as the avalanche angle. Those tests are suitable for assessing materials with cohesive interaction and are often assisted by video imaging [16].

Laser absorptivity

Absorptivity (A) is the fraction of the incident radiation effectively absorbed by a material. It is indirectly determined by measuring the reflectance (R), which corresponds to the fraction of the incident radiation that is reflected and, therefore, not absorbed by the material [17]. Only a fraction of the energy is absorbed by the surface of the particles and penetrates the powder bed, while the other fraction is reflected [7, 18].

Assuming that the transmittance is negligible for metallic alloys, A is calculated by $A = 1 - R$. In general, absorptivity depends on laser wavelength, material composition, surface geometry, ambient gas, and temperature, among other factors [17].

Powder absorptivity can be measured using the experimental setup shown in Fig. S3 (Supplementary Material). A laser beam passes through a modulator and couples the loose powder surface through an optical system [17]. The powder remains inside a cuvette full of particles localized in the center of the integrating sphere [17]. Consequently, the powder reflects the radiation and is integrated by the sphere, arriving at a photoreceiver [17]. Finally, the photoreceiver detects the signal, which varies proportionally with the reflected radiation intensity and is registered by a digital processing oscilloscope [17].

The energy absorption capacity of powders is exceptionally relevant in AM processes. Absorptivity depends on alloy composition and powder characteristics, which affect the quality of the final parts. Aluminum powders have high reflectivity, which can reach up to 77 and 91 % of the energy supplied by Nd:YAG ($\lambda = 1.06$ μm) and CO_2 lasers ($\lambda = 10.6$ μm), respectively [19]. Copper alloys also display high reflectivity for both

Nd:YAG and CO_2 lasers, which motivates the use of lasers with a shorter wavelength, such as blue ($\lambda = 0.450$ μm) and green lasers ($\lambda = 0.515$ μm) [20]. In contrast, reflectivity values obtained for other materials, such as AISI 316L stainless steel (41 %) [21] and the Ti–6Al–4V alloy (53–59 %) [22] are considerably lower, favoring a more extensive processing window. Notably, the effective absorbance also depends on the particle size, and the energy that can reach the underlying layer depends on its density.

Laser incidence on the powder promotes energy absorption and reflection, and the latter also contributes to the first because the reflected beam is redirected to other particles [23]. As powder particle size increases, energy absorption decreases because the number of reflections directed to other powder particles decreases, resulting in lower energy efficiency [24]. It has been shown that the reduced powder particle size used in AM processes enables more significant consolidation of the superimposed layers and requires lower heat input to melt and weld the powder bed because of the higher absorbance [25]. Moreover, smaller particles have a higher surface-per-volume ratio, increasing reflectivity, and are likely to evaporate because of their lower mass and higher laser absorptivity [26]. Processing coarse powders by L-PBF results in the formation of thicker layers and, consequently, the energy reaching the underlying surface decreases, affecting interlayer weldability [27].

Apparent and tapped density

Apparent density is the mass-to-volume ratio expressed in g/cm^3, whereas tapped density is a function of powder size distribution, morphology, and surface roughness [28]. In both techniques, a powder volume must occupy a specific container with a known volume. In the apparent density technique, the container has a volume of 25 cm^3, and the powder must fill it freely only by gravity. In the tap density technique, a specific test portion of powder mass fills the graduated glass cylinder, and it is then tapped or vibrated until complete densification or until there is no further decrease in volume [28]. The apparent density of metallic powders can be measured according to standardized methods such as Hall flowmeter/funnel for free-flowing powders (ASTM B212), Carney funnel for non-free-flowing powders (ASTM B417), Scott volumeter (ASTM B329), and Arnold meter (ASTM B703). The tap density of metallic powders is determined according to the ASTM B527 standard. Tap density is usually higher than apparent density, and the difference greatly depends on particle shape and size [28]. Thus, higher friction forces (small particles, irregular morphology, and rough surface) give rise to higher tapped density because vibration assists with better accommodation of the particles [28]. For example, spherical copper powders present a difference of 18 % in the comparison between apparent and tapped density, while this difference increases to 35 % for irregular copper powders [29].

Skeletal density is detailed by the ASTM B923 standard test method and is measured by helium or nitrogen pycnometry. It provides the true density of metal powders. Skeletal density is essential to determine the internal porosity within the particles and does not depend on the flowability and packing capacity of the particles.

Optimizing the layer density is fundamental to ensure a high density of the final part [7]. Even a low degree of inhomogeneity may result in porosity or incomplete layer melting [30]. Thus, the powder's main characteristics for forming a dense and homogeneous layer are discussed. AM processes usually use powders with an optimal particle distribution between 10 and 100 μm in diameter. Small particles are essential in filling the spaces between larger particles, increasing powder density, and improving surface roughness. Small particles also tend to agglomerate due to the attracting short-range forces, and because of their larger surface area, they have a more significant effect on interparticle friction, harming the flow behavior, and promoting poor powder spreadability [31]. Therefore, the powder should present a limited number and size of small particles so as not to deteriorate the flowability [16]. A study conducted with aluminum alloys identified a different flow behavior when many small particles were present. In the presence of many small particles, many surface imperfections in the form of holes were present. Fine particles tend to generate agglomerates that reduce the fluidity of the powder and, consequently, favor the formation of defects in the built parts [32].

In contrast, larger particles flow more freely than smaller ones. However, large particles tend to increase surface roughness because of the difficulty of achieving complete melting, thus decreasing the printing resolution [16, 30]. Furthermore, a spherical shape is preferred because it promotes less particle friction. It leads to free-flowing particles and tends to arrange more efficiently than irregular shapes [31]. Smoother surfaces are desired to provide reduced interparticle friction. Moreover, clean and dry surfaces prevent agglomeration due to unwanted bonds between particles. The bonding results from the action of capillary forces in the presence of moisture, which interferes with particle motion [30, 33].

The powder PSD is an important parameter to ensure good final part quality. The upper limit to determine the size range is defined based on the thickness of the powder layer, as shown in Fig. S4 in the Supplementary Material. If the layer thickness is smaller than the maximum particle size, the larger particles will be segregated, and the smaller ones will be preferentially deposited into the build volume [34]. However, increasing layer thickness decreases layer density resulting from the larger voids developed between the particles (Fig. S4). Besides the size range, PSD is decisive in particle packing and, consequently, in the powder bed process. It is essential to tailor the PSD to smaller particles filling the voids between the larger ones [6].

Furthermore, fine particles increase the laser's absorption capacity and reduce the built parts' surface roughness [26].

Different types of defects can develop during AM processing. Some originate from process parameters, and others from the feedstock. Porosity in the produced parts can result from the powder porosity or be caused by flowability and packing issues during AM [35]. Internal powder porosity arises from trapped atomization gas, leading to larger pore size and microporosity in interdendritic regions, originating during solidification. These defects become more frequent in the presence of particles with diameters greater than 70 μm. No post-processing treatment can remove porosity arising from feedstock powder [35].

Poor flowability and low packing efficiency are due to powder agglomeration and satellite particles. Characterizing the total porosity volume, distribution, and shape of the pores in the built parts is essential to determine the minimum pore fraction associated with the best processing parameters. Powder morphology can influence energy absorbance. Less irregular morphologies favor increased energy absorbance and reduced energy reflection [27]. The formation of oxide layers on the surface of the particles can increase absorbance; that is why powders produced by water atomization require less energy input during melting [27, 36, 37].

Powder production

Several manufacturing techniques are applied to produce metal powders [29]. The choice of method should be related to the application and desired properties because each technique yields powders with different morphology, shape, and size [16, 29]. Some of the methods are classified as follows [29]:

Chemical: chemical reduction and decomposition of compounds;
Physical: electrolytic process and atomization;
Mechanical: ball milling and vortex milling (both including impact, attrition, shear, and compression).

According to Popovich and Sufiiarov [38], gas atomization is the most widespread technology for the mass production of metal powders in AM. It was supported by other studies that highlighted that atomization is one of the most common methods to produce powders for AM technologies since any liquid can be broken into droplets [28].

Atomization

The principle of atomization is the disintegration of a thin stream of molten metal by subjecting it to an atomizing medium, e.g., gas (gas atomization), water (water atomization), and plasma (plasma atomization) [38]. During the impact, the molten metal is divided into droplets, which rapidly solidify in flight before they reach the atomizer walls (at cooling rates in the 10^2–10^7 K/s range) [38].

Atomization processes can produce spherical powders with narrow PSD, which is essential for obtaining repeatable and reliable results during AM [39]. Moreover, these characteristics are achieved immediately after powder synthesis, while other processes need additional steps to achieve the desired morphology [39]. Although atomization produces spherical metal powders, it is crucial to eliminate atomization debris (splats and fibrous remains of the non-steady state startup period), for instance, through sieving. In addition, Dawes et al. [30] suggested that none of the powder production technologies reach a production yield of 100 % in the required size fraction; thus, post-processing is usually necessary. The as-produced metal powder must present a well-defined PSD suitable for the required AM processes [30].

Water atomization is simpler and cheaper than gas and plasma because of its atomizing medium, lower pressurization energy (compared with gas atomization), and high productivity [40]. It consists of water jets (pressurized at 5–13 MPa) symmetrically positioned around the stream of liquid metal that atomizes and solidifies as fine particles [30, 33, 40]. Finally, the powder is collected from the bottom of the chamber [30]. Some additional processing steps are required to dry the powder [30]. Particles with sizes ranging from 5 to 500 μm (D_{50} = 100 μm) with irregular morphologies are obtained, which disadvantages high packing density and flow properties [30, 33, 40]. Water atomization is only suitable for non-reactive materials, and a significant part of the produced powder presents irregular morphology.

Gas atomization is usually the choice to produce AM feedstock [30, 33]. The method is similar to water atomization, but gas is used instead of water at pressures that range from 350 kPa to 4 MPa [30, 33, 40]. Air is commonly used as the atomizing medium, but inert gases (nitrogen, argon, or helium) may also reduce the metal's risk of oxidation and contamination [30, 33]. The obtained powder has a more spherical morphology than that produced by water atomization, and its particle size can vary between 10 and 300 μm (D_{50} = 80 μm) [39, 41]. When an inert gas is used, the oxygen content is ~ 100 ppm (0.01 %), which meets the requirements for use as AM feedstock [39, 41, 42]. Figure 4 compares powders produced through gas atomization and water atomization, respectively; the morphological difference between the powders is evident.

The most common technique employed to produce powders of pure titanium and its alloys is plasma atomization, developed by PyroGenesis Canada Inc. [44]. The atomizing medium is composed of plasma torches focused on a metal wire. Thus,

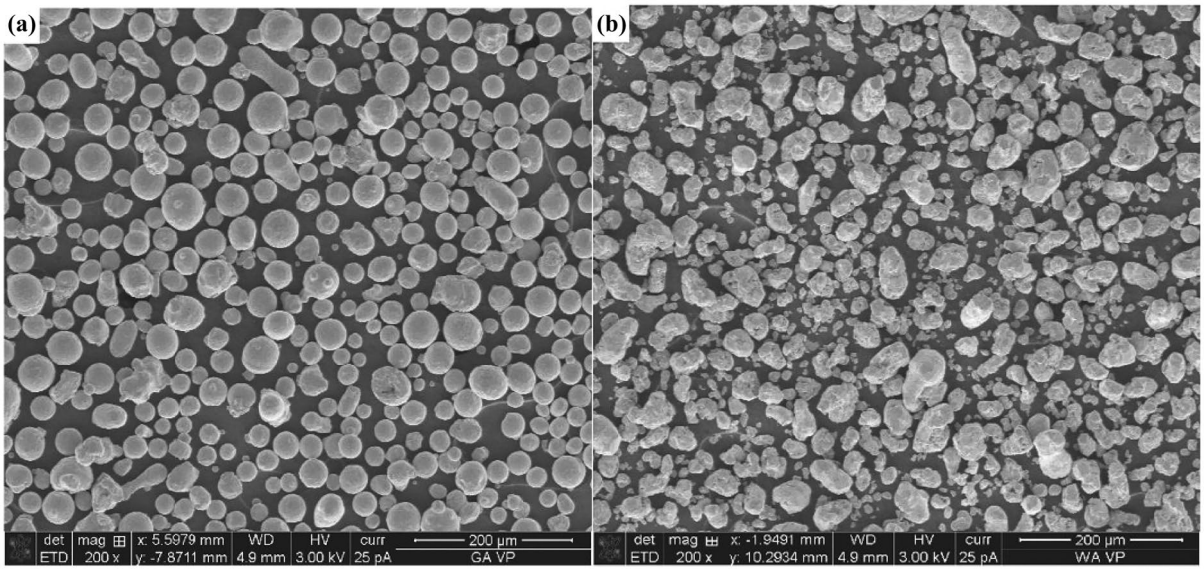

Figure 4: SEM image showing the morphology of low alloy steel powders obtained by (a) gas atomization; and (b) water atomization. *Reproduced under the terms of the Creative Commons CC-BY license* [43].

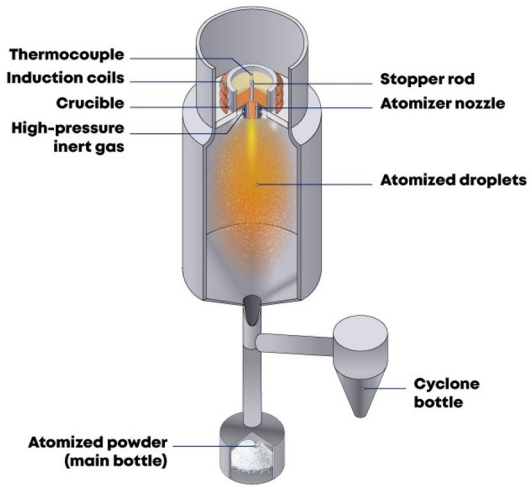

Figure 5: Schematic illustration of a gas atomizer and its main auxiliary components. *Reproduced with permission from Ref.* [9].

the metal is melted, and the material is atomized [44]. Plasma atomization yields particles with a highly spherical shape, no satellites, no contamination, narrow PSD, and an average particle size of 40 µm [42, 44]. However, the process is expensive and has low productivity, and because of this, some alternative techniques are used [44].

Figure 5 shows a detailed schematic diagram of a gas atomizer. The first step in the process is to melt the metal. The material is placed inside a crucible and melted by induction heating [45]. A thermocouple is used to measure the temperature of the molten metal. When the melt reaches a predetermined temperature (superheat temperature), it is led through the exit into the atomization chamber when the stopper rod is pushed upwards [45]. When the molten material reaches the atomization chamber, it is disturbed by gas jets at high pressure; consequently, a spray is formed, and the particles solidify, forming the metal powder. Finally, the powder can be obtained from the collector. As previously explained, not all of the material is transformed into powder because of the formation of atomization debris and splats. Therefore, a post-process must select only the particles that can be processed, for example, by AM [30]. In some gas atomizers, another collector localized on the side (and not below, as in other devices) collects the smaller particles, i.e., the powder undergoes the first separation automatically by the collection system.

For reactive materials such as aluminum, there is a need to perform an extra step before removing the atomized powder from the collector [46]. These materials must undergo a "passivation process," i.e., the particles are exposed to a controlled oxygen environment, and oxides form on the surface [46]. Consequently, the chances of explosion in post-atomization processes are decreased because the chemical stability of the powder is increased [46]. For example, after the atomization of the AlSi10Mg alloy, the powder was submitted to a passivation process in Ref. [47]. A nanometric oxide layer (~5 nm) was formed on the surface of the particles when exposed to the controlled oxygen environment.

Modeling of the gas-atomization process

It is not difficult to understand how gas atomization works, but numerous physical phenomena and interactions occur during the process. Several researchers have suggested mathematical models, equations, and theories to understand the technique

comprehensively [28, 40, 48–50]. There are several interrelated phenomena and material variables involved, e.g., gas jet distance and pressure, gas velocity and mass flow rate, metal velocity and mass flow rate, nozzle geometry, angle of impingement, superheat temperature, metal surface tension, and metal melting temperature range [51]. Different studies have been carried out to predict the distribution of particle sizes and shapes as a function of the process parameters and material properties [10, 51]. Studies show that as gas pressure or mass flow rate increases, the gas jet to metal stream distance decreases, and the average particle size diameter decreases [10, 51].

The influence of different parameters on gas atomization outcome is demonstrated by the Lubanska equation (Eq. 5), which correlates process parameters, material properties, and average particle size [10, 51]:

$$\frac{D_{50}}{D_{\mathrm{FM}}} = K * \left[\frac{\upsilon_{\mathrm{m}}}{\upsilon_{\mathrm{g}}} * \frac{1}{\mathrm{We}} * \left(1 + \frac{M}{A}\right)\right]^{\frac{1}{2}}, \tag{5}$$

where 'D_{FM}' is the diameter of the liquid metal stream, 'K' is a constant which depends on the equipment, 'υ_{m}' is the kinematic viscosity of metal, 'υ_{g}' represents the kinematic viscosity of the atomizer medium, 'We' is the Weber number (Eq. 6), 'M' is the mass flow rate of liquid metal, and 'A' is the mass flow rate of the atomizer medium [10].

The Weber number (Eq. 6) describes the liquid metal stability and shows the ratio between the inertial forces ($\rho * V^2$) and surface tension forces ($\frac{D_{\mathrm{FM}}}{\sigma}$) [51, 52]:

$$\mathrm{We} = \frac{\rho * V^2 * D_{\mathrm{FM}}}{\sigma}, \tag{6}$$

where 'ρ' is the density of the liquid metal, 'V' represents the relative velocity between the atomizer medium and liquid metal, and 'σ' is the surface tension of the liquid metal [51, 52].

The Lubanska equation also includes the liquid metal (M) and gas (A) mass flow rates, and they can be calculated using Eqs. 7 and 8, respectively:

$$M = a_{\mathrm{m}} * \rho_{\mathrm{m}} * \left[2gh + \frac{2 * \Delta P}{\rho_{\mathrm{m}}}\right]^{\frac{1}{2}}, \tag{7}$$

where 'a_{m}' is the liquid metal exit area, 'ρ_{m}' represents the density of liquid metal, 'g' is the gravitational acceleration, 'h' is the height of liquid metal in a crucible, and 'ΔP' is the pressure difference between the crucible and the atomization chamber [53].

$$A = a * \left(\frac{2}{k_t + 1}\right)^{\frac{k_t+1}{2(k_t-1)}} * \frac{P * \sqrt{2g}}{\sqrt{RT}}, \tag{8}$$

where 'a' is the gas exit area, "k_t" represents the ratio between the specific heat capacity of an atomizing gas at constant pressure and the specific heat capacity of the atomizing gas at constant temperature (C_p/C_v), "P" is the gas pressure, "R" is the gas constant, and "T" is the gas temperature [53].

According to the Lubanska equation and literature data, some parameters are more significant [10]. For example, an increase in superheat temperature can influence both PSD and D_{50}, because it will cause a decrease in the surface tension and viscosity of the metal; consequently, the metal stream would be broken more easily by the atomizer medium [52]. Figure 6(a) presents the influence of superheat temperature on the gas atomization of Cu powders with nitrogen as a medium atomizer. Higher temperatures result in finer particles, and the PSD is also affected.

The superheat temperature cannot be exaggerated, as it may cause evaporation of alloying elements, damage the equipment, and cause undesirable reactions between the crucible and the melt [48, 55]. Thus, the superheat temperature must be intermediate to avoid premature metal solidification and unwanted effects (evaporation, damage, and reactions). According to the literature, the usual range of superheat temperature is 75–150 °C, although higher temperatures have been reported [52].

A study by Lubanska showed that the metal exit area (also called nozzle diameter) influences the produced powders [10]. Gao et al. also demonstrated it in a study with different nozzle diameters [56]. They suggested that particles with a higher average size would be produced for a higher nozzle diameter, but smaller particles are yielded when a smaller nozzle diameter is used. Therefore, nozzle diameter and particle size are directly proportional [56]. In Fig. 6(b), it is possible to observe the changes in D_{50} of an AlSi10Mg alloy gas-atomized powder as a function of nozzle diameter.

Yet, a different study highlighted the difficulty of decreasing the diameter indefinitely [14]; it was suggested that high resistance forces appear when the nozzle diameter is reduced. In some cases, additional driving forces are required for the liquid metal to flow using a small diameter. In Ref. [14], the authors used a pressure increment in the melt chamber to facilitate the molten liquid flow to the atomization chamber. In the Lubanska equation, the liquid metal exit area influences the liquid metal mass flow rate. Thus, if a greater diameter is used, the liquid metal mass flow rate will increase, which results in a coarser powder [10].

Gas pressure is another crucial process parameter in Lubanska's equation and the gas mass flow rate calculation, Eqs. 5 and 8, respectively. Both equations show that particle sizes obtained by gas atomization are reduced with increasing gas pressure [Fig. 6(c)] [10, 53]. Ünal [50] suggested that liquid metal mass flow rate decreases with increasing gas pressure; consequently, a higher gas-to-metal ratio (GMR = A/M) is obtained, which reduces the average powder particle size. However, as demonstrated by Allimant et al. [57],

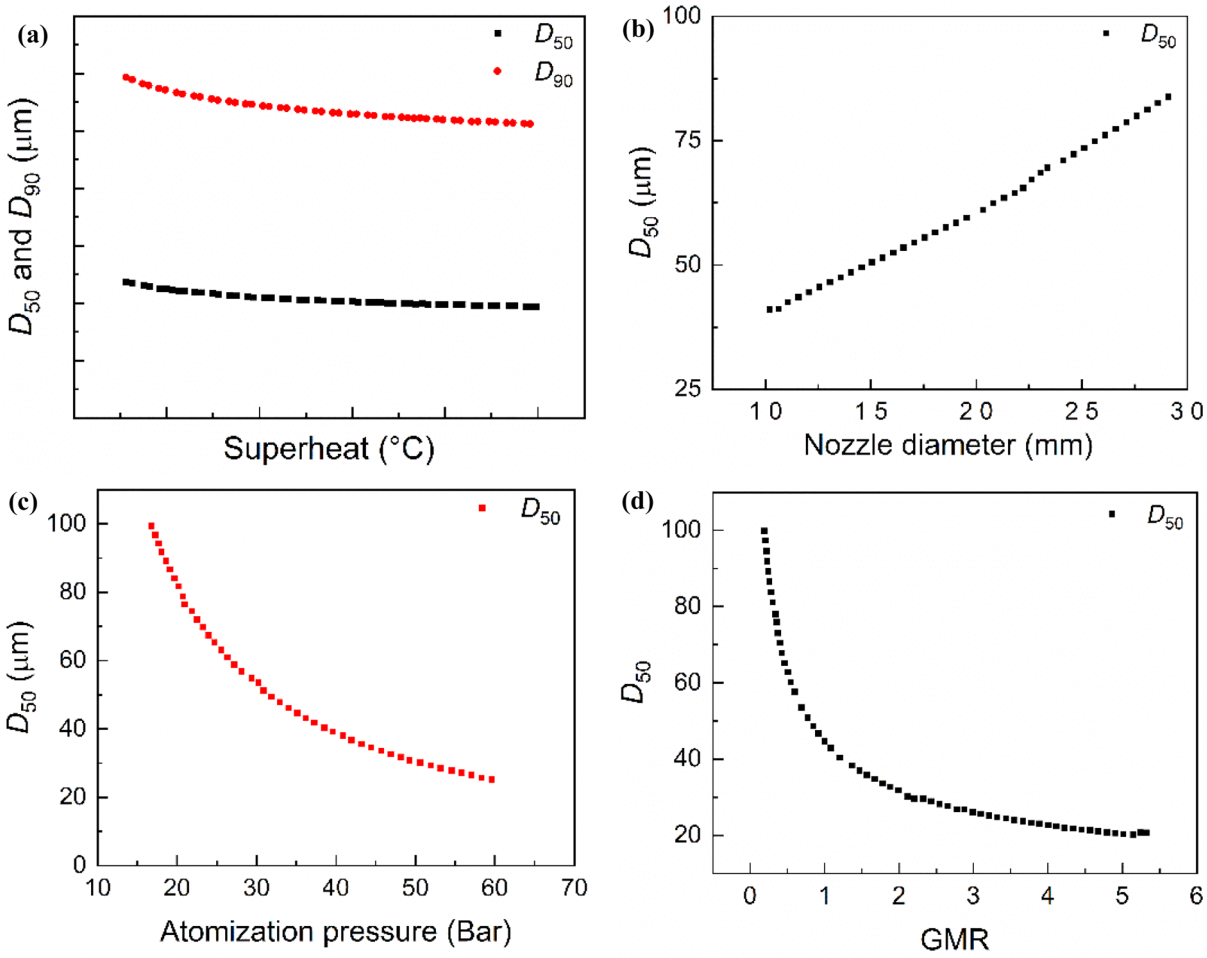

Figure 6: (a) D_{50} and D_{90} percentiles of gas-atomized Cu powders as a function of superheat temperature; (b) D_{50} of gas-atomized AlSi10Mg powders as a function of nozzle diameter; D_{50} of gas-atomized Cu powders as a function of (c) atomization pressure; and (d) GMR. *Reproduced and adapted with permission from Refs.* [14, 54]. *Reproduced under the terms of the Creative Commons CC-BY license.*

intermediate gas pressure is recommended because (i) high gas pressure reduces melt velocity and could freeze the metal before it reaches the atomization chamber, and (ii) small gas pressure produces coarser powders. Other important factors that influence gas atomization are the type of gas used (He, Ar, or N_2), gas temperature, and nozzle design (free-fall nozzle, close-coupled nozzle, De Laval nozzle) [45, 55, 58, 59].

New equations and modifications of the Lubanska equation were proposed in the literature to predict D_{50} in different atomizers since Lubanska considers a free-fall type nozzle [54, 60]. However, these equations (including the Lubanska equation) use GMR as an input parameter, which is difficult to calculate because both gas and metal mass flow rates are obtained through empirical equations. These equations do not consider backpressure, which occurs in the close-coupled gas atomizer and can influence the GMR [54, 60]. Probably, the development of new equations and refinement of existing ones may help to optimize the gas-atomization process, increasing the yield of powder production in the particle size range of 10–105 μm (considering particle size range 10–45 μm for L-PBF and 45–105 μm for DLD) [35, 60]. Currently, the rate of powder yield useful for the L-PBF process is between 45 and 85 % [35, 60].

Other methods

Although gas atomization is considered the most suitable method to produce metal powder to be applied in AM, several studies have pointed out the method's drawbacks [61, 62]. The main issues are the high energy consumed during gas atomization and the high costs involved due to energy consumption, consumables, and equipment [61, 62]. Therefore, alternative routes to produce feedstock, which consider environmental and sustainable aspects, must be explored to attain the sustainability of AM [62].

An alternative route is ball milling, a process conducted at room or cryogenic temperatures to transform coarser powder

into finer powders [62, 63]. Ball milling involves a rotating vial containing metal (or ceramic) balls together with the material to be processed (e.g., metal powder) [61]. The vial is rotated, which makes the balls interact with the material, and thus, the morphology and size of metal particles are changed due to abrasion and impact phenomena [62, 64]. The milling process can be enhanced by incorporating hydrogen into the alloy before ball milling, making it more susceptible to cracking instead of deforming, and afterward, the alloy is dehydrogenized. The cycle of hydriding-milling-dehydriding is referred to in the literature as HMD [65].

Some studies suggested using the ball milling route to recycle metallic waste, such as machining chips of aluminum and copper alloys, stainless steel, and titanium alloys [66, 67]. They showed that it is possible to achieve powders with the required properties and characteristics to be applied in AM [61, 62]. In section "Metal powder for additive manufacturing", an example of ball-milled powders used in AM process will be shown.

Another method for producing powder suitable for AM processes is the plasma rotating electrode process (PREP), which results in particles with higher circularity and smoother surfaces than GA, as shown in Fig. 7 [68]. In PREP, the material is melted by a plasma directed against the surface of a rotating anode, which pulverizes the molten stream forming highly spherical particles. The main downside of PREP is the high cost of the process and its higher productivity rate with coarser PSD (50–350 μm) when atomization processes are more suitable to produce finer particles on a large scale [69]. Despite their high costs, PREP powders are indicated for applications where chemical contamination must be avoided because ceramic inclusions may contaminate atomized powders due to the interaction of the molten metal flow with the ceramic nozzle and its consequent erosion [70].

Metal powder for additive manufacturing

This section overviews the powder characteristics suitable for L-PBF and DLD processing focused on aluminum alloys and steels. Studies focused on powder behavior are presented and discussed for each class of process and material. In the Supplementary Materials, Table S1 containing a summary of the related data is given.

Powder feedstock for laser powder bed fusion

The initial step in L-PBF consists of spreading a small amount of powder from the hopper (a rake or roller system) across the build chamber to form a thin (no more than one to two-particle

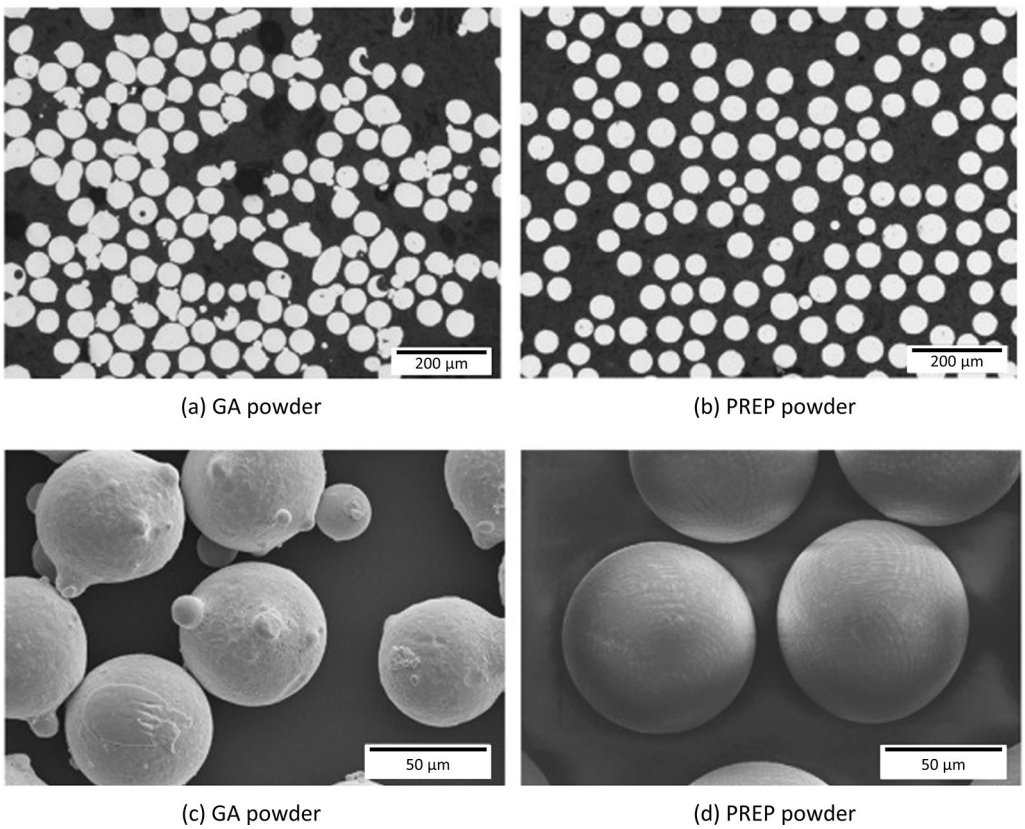

Figure 7: Cross-section (a, b) and SEM surface image (c, d) of Inconel 718 powders produced by gas atomization (GA) and plasma rotating electrode process (PREP). *Reproduced and adapted with permission from Ref.* [68].

diameters) continuous powder layer [30]. L-PBF processing requires good flowability and high apparent density of the deposited layer [31]. The quality of a component built by L-PBF is assessed based on part density, mechanical properties, surface roughness, dimensional accuracy, and build rate [30]. Powders with spherical particles and narrow PSD are commonly preferred as starting feedstock. However, each process requires a specific PSD, typically 15–45 μm for L-PBF [30], making the feedstock cost for the AM parts higher [7].

One of the first studies [71] on the influence of powder particle size in AM involved selective laser sintering (SLS), a process similar to L-PBF but in which the material does not melt. The process is also named direct metal laser sintering (DMLS). Water-atomized iron powders were used to analyze the effect of mean particle size on sintering behavior. The D_{50} investigated was in the range of 13–175 μm. Powders with different D_{50} and PSD have distinct behaviors; however, comparing the relative densities of the parts produced with the different process parameters, the highest density was obtained for a scan rate of 50 mm/s and a hatching distance of 0.2 mm. The highest part density was obtained with powders having a D_{50} of 30 μm. It is expected that the smaller particles tend to enhance the densification kinetics. However, the results showed that powder densification with D_{50} of 13 μm was lower than for powder with a median particle size (MPS) of 30 μm. One of the reasons is the powder agglomeration of the smallest particles, which dramatically increases the reflectivity of the powder bed. It is also related to the surface chemistry and shape of the coarser powders, which had an irregular morphology and higher oxygen and carbon concentrations. Hence, the densification of the built parts increased with decreasing the particle size, except for very fine powders (MPS < 20 μm) [71].

Several studies have assessed the influence of D_{50} on the density of printed parts. It has been verified that fine powders require lower energy density to achieve higher-density parts and better surface quality [23]. One of the studies analyzed the influence of three grades of AISI 316L stainless steel gas-atomized powders with D_{50} of 15, 28, and 37 μm and D_{90} of 31, 41, and 60 μm. All powders achieved densities > 99 % after adjusting the energy density. Powders with larger particles might have larger pores, thus compromising mechanical strength while providing ductility benefits [23]. Few small particles are needed to optimize part properties such as density, surface quality, and mechanical strength, whereas large particles are limited according to layer thickness [23]. In addition, the effect of particles < 15 μm in AISI 316L stainless steel powder was analyzed. The powders considered had particle sizes < 45 μm and 15–45 μm ranges, and D_{50} around 27 and 29 μm, respectively [72]. The results showed that powders with a broader range of PSD yield higher-density parts with a smoother surface finish under lower laser energy intensity, whereas a narrower range provides better flowability, higher ultimate tensile strength (UTS), and hardness [72]. Another study analyzed the same material with the same PSD, 10–45 μm, and achieved higher yield strength with the same manufactured parts elongation [73].

The effect of layer thickness was also the subject of studies. Powders with $D_{50} = 46$ μm and $D_{90} < 106$ μm were assessed by L-PBF technique using powder layer thicknesses of 30 μm, 50 μm, and 70 μm [34]. The layer thickness limits the larger particles. If the particles are larger than the layer thickness, segregation will occur in the L-PFB process. In the case of thick layers (> 50 μm), larger particles, in addition to decreasing the layer density, tend to incomplete melting, porosity, or micro-cracking, causing decreased strength and elongation (ductility). Considering the particle size range, the best layer thickness was 30 μm as the mechanical properties were superior to the others [34]. A correlation was observed between the density of the deposited layer and the built parts, where an increase in the density of the deposited powder layers generates a higher density of the components [74].

Pasebani et al. [8] studied the feasibility of applying 17-4PH stainless steel powders manufactured by water atomization to construct parts by L-PBF. The water-atomized powders had an irregular shape, $D_{50} = 43$ μm, and higher oxygen content, while gas-atomized powders had a spherical shape, $D_{50} = 13$ μm, and higher nitrogen content. Gas-atomized powders showed the highest apparent and tapped densities and a Hausner ratio of 1.324, while the ratio was 1.301 for water-atomized powders, indicating slightly better flowability for the gas-atomized powders. L-PBF parts produced with water-atomized powders also obtained an optimal density reaching values > 95 %, similar to parts built using the gas-atomized feedstock. Nevertheless, because of the particularities of each powder, the energy density had to be adjusted to higher values for the water-atomized powder. Mechanical properties such as hardness, yield strength, and UTS were comparable to those of gas-atomized and wrought alloys, presenting water-sprayed powders as a promising alternative for producing L-PBF parts because of their lower production costs [8]. Studies have also shown a strong dependence of densification and mechanical properties on energy density in L-PBF processing. Samples prepared using gas-atomized powders have superior properties when processed at low energy densities. However, water-atomized powders produced L-PBF parts with densification and properties comparable to gas-atomized powders with high energy density [8].

The effects of two atomization processes on particle morphology and chemistry were analyzed for Fe–Cr–Mo, Fe–Cr–Mn and Fe–Cr–Mo–Mn–Ni low-alloyed steels. The gas-atomized powder showed enhanced flowability and lower oxygen content than the water-atomized powder. The Hall flow rate was significantly higher for the gas-atomized powder than

for the water-atomized powder: 12 and 28–36 s, respectively. The apparent and tapped density values were even higher: 4.36 and 5.05 g/cm^3 for the gas-atomized powder and 2.70–2.80 and 3.39–3.62 g/cm^3 for the water-atomized powder. In both cases, it was possible to achieve relative part density values > 99 %, but the gas-atomized powder generally showed higher densities [75].

Marchetti and Hulme-Smith [15] evaluated a variety of steel powders with different compositions, atomization routes, and particle size ranges. The powders were dried to remove moisture content before testing to avoid humidity. In cases where frictional forces dominate, powders may not flow regularly, and an arch may be formed near the funnel outlet, which can lead to the presence of vertical cavities known as ratholes or jamming, where the powders have their flow stopped, as shown in Fig. S5 (Supplementary Material) [76]. Ratholes and jamming are observed when the powders are cohesive, the orifice diameter ratio of the funnel to the particle diameter is too small, or the PSD is too broad [15]. The results revealed that all powders with $D_{50} < 27$ µm could not flow, including the gas-atomized powders, and ratholes and jamming were observed [15]. The other powders had Hall flow rates between 11 and 12 s for 50 g of powder, except the coarser powder ($D_{50} = 75$ µm), which was 21 s [15].

The funnel method uses gravity force to flow the powder through an orifice. Because the density of aluminum alloys is ~ 2.7 g/cm^3 and that of steels is ~ 7.8 g/cm^3, steels flow more easily. Although aspects like preferred powder morphology, particle size, and layer thickness can be generalized regardless of material, other points must be detailed. Sercombe et al. [77] explored some inherent difficulties working with aluminum powders. They showed how laser melting of aluminum poses several challenges to producing high-density components because of powder characteristics (stability of the oxide layer, poor flowability, high reflectivity, and high thermal conductivity) [77]. Furthermore, aluminum alloys generally present a wide solidification temperature range, which generates defects that reduce the mechanical properties of final parts and hinder the fabrication of satisfactory components [78].

To overcome these challenges, aluminum alloys (mainly the 2XXX and 7XXX series) require different methods, such as optimization of the processing parameters, alloy composition, and processing environment, to fabricate parts by L-PBF [79, 80]. For example, after these optimizations, aluminum alloys of the 2XXX and 7XXX series, which are heat-treatable, displayed good mechanical properties, comparable with Al alloys fabricated by conventional methods [81].

Li et al. [82] reported an enhancement in the densification of the Al–12Si alloy processed by L-PBF via powder drying. Previous studies have shown that porosity could not be avoided entirely in Al–12Si L-PBF-built parts simply by optimizing processing parameters, and similar results have been found for other alloy systems [82–85]. The powder was dried before being processed by L-PBF, and an increase in the relative density of the produced parts (≥ 99 %) in comparison to components processed from the as-received (non-treated) powder was observed [82]. This was attributed to the powder surface modification after removing the moist skin during drying. Thus, the formation of harmful oxides and hydroxides forming during L-PBF was prevented [82].

Adding to the study's findings above, Riener et al. [47] identified the influence of storage conditions considering the powder and its behavior as feedstock. They tested different storage conditions and investigated their effect on the L-PBF final parts [47]. Their results showed that built parts from powder stored under humid conditions presented lower density and mechanical strength [47]. In addition, they suggested that the problem could be reversed by drying the powder in a vacuum drying oven, as also recommended by Li et al. [82].

Powder feedstock for direct energy deposition

While L-PBF requires a particle size range of 15–45 µm, DLD requires a larger size range, typically between 50 and 200 µm. A larger PSD allows more outstanding flowability and reduces the formation of defects such as agglomerations in DLD [86].

The literature addressing the development of powders for use in DLD shows that steel powders, especially stainless steel powders, are frequently applied to evaluate the feasibility of the process. An important example is the evaluation of the feasibility of reusing the AISI 316L stainless steel powder used in DLD processes, as reported by Li et al. [87]. They verified that the powder can be used after more than one cycle of DLD without significantly affecting the final properties of the printed part despite a slight shift in PSD [87]. This result corroborates the findings reported in a previous study [86].

There is a research interest in evaluating the feasibility of less-spherical powders as feedstock for DLD, aiming at an overall cost reduction and the need for gas-atomized powder. Pinkerton et al. [88] reported that water atomization is a promising alternative in a study using a coaxial nozzle to blow H13 steel powder into a laser-induced melt pool on the H13 steel part surface. The following values were obtained for the gas-atomized and water-atomized powders: D_{50} of 71 and 65 µm, the reflectivity of 82 and 69 %, and an apparent density (tapped density) of 59 and 38 %. Samples printed with 800 W power using gas-atomized powder showed higher surface roughness values than those of samples using water-atomized powder. Still, this relation was inverted as the laser power was decreased to 600 W. Both types of powder exhibited a linear dependence of surface roughness on laser power. The gas-atomized powder samples showed higher hardness, probably resulting from a lower transition temperature in the melt pool, which led to a more significant martensite volume fraction. Despite the differences,

most of the process characteristics were similar for both powder types, which led those authors to consider water-atomized powders an alternative with better cost–benefit than gas-atomized powders [88].

The literature also reports on the viability of using mechanically generated powder instead of gas-atomized powder in DLD. Since ball milling equipment is cheaper than an atomization station, mechanically generated powder enables more flexibility and offers greater feedstock diversity for DLD processing. The use of ball-milled AISI 316L stainless steel powder in DLD was reported by Jackson et al. [89]. The gas-atomized 316L powder had a reduced Hall flow rate than the ball-milled 316L powder, which directly impacted the surface roughness of the printed part, as illustrated in Fig. S6 in the Supplementary Material. The relative density and reproducibility were also negatively affected. However, the ball-milled feedstock leads to relative densities up to 99.8 %, evidencing that mechanically generated powder can be effectively used in DLD processing.

Results have shown even more promising by adjusting the milling process to obtain spherical particles and a more controlled PSD. An example of such adjustment of the milling process was reported by Fullenwider et al. [62], who obtained near-spherical particles from stainless steel machined chips by adding a second step to the ball milling process. The sphericity of the particles obtained through the two-step milling process was higher than that of the single-step milling process with the same duration. In addition, the excellent surface quality of single tracks printed using the two-stage milled powders indicates that this type of powder can be used to print high-quality parts.

The intrinsic characteristics of aluminum alloys, exceptionally high conductivity, and thermal reflectivity reduce their application in DLD processing. Gas-atomized AlSi10Mg alloy powders were processed by DLD using a Nd:YAG laser source [90]. The particle size was used as the criteria to separate the powders into three different groups: < 40 µm, 40–63 µm, and 63–75 µm. The parts were built using laser powers of 2, 4, and 6 kW and a constant powder feed of 4 g/min [90]. The feeding system behavior was also verified with the laser off, a condition referred to by the authors as 0 kW. The thermodynamic simulations and image analyses showed that the smaller particles promote higher density when entering the laser focus, allowing greater energy absorption, as shown in Fig. 8. Nevertheless, an increase in the power supplied generated the disintegration of the particles resulting from an excessive increase in heating rate ($> 10^9$ K/s), and a greater degree of thermal expansion of the particles (up to 11.44 %) [91]. It occurs because the surface tension of the metal is insufficient to hold the particles together, favoring back pressure [92]. A correlation was observed regarding the number of disintegrated particles in the three groups of powders, with the highest disintegration values found in particles > 63 µm. In addition to their higher specific surface area, the more significant heating of small particles was mainly due to higher concentration and better distribution within the laser focus, favoring a more considerable energy input [90, 93]. The increased number of disintegrated particles generated a loss of power and absorbed energy [94].

The addition of inoculants to powders has also been studied. Inoculants such as SiC (20 nm) and TiC (40 nm) were added at 3 wt. % to AlMgScZr powders through high-energy ball milling before processing by DLD [95]. An increase in the milling time produced greater porosity of the AM parts due to the change of the typical spherical geometry of gas-atomized

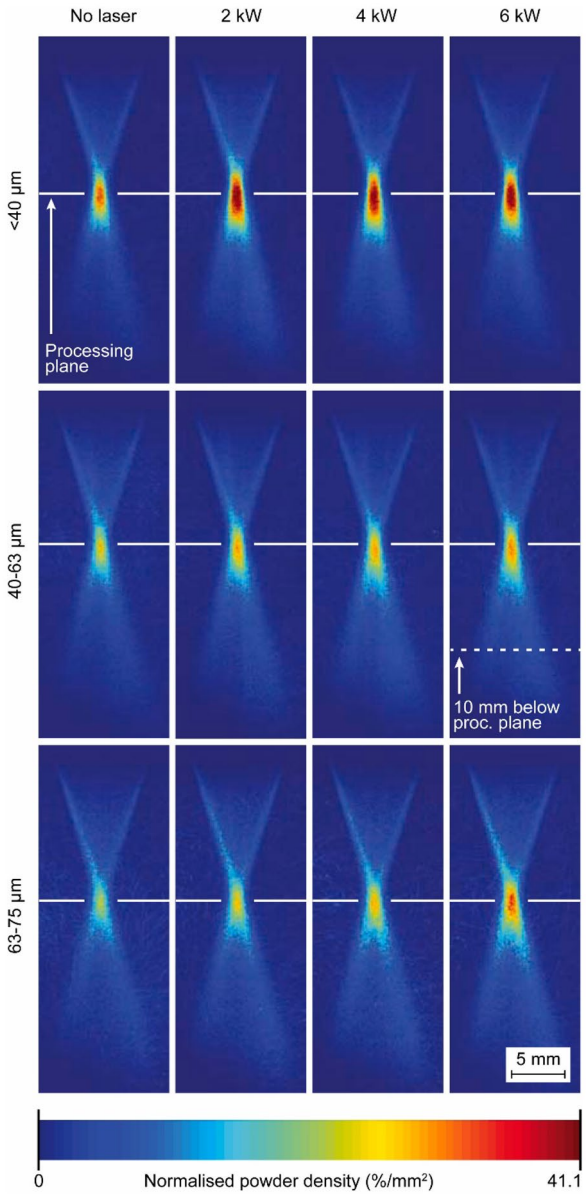

Figure 8: Powder density as a function of the particle size for the DLD process. *Reproduced under the terms of the Creative Commons CC-BY license* [90].

powders and the agglomeration of the particles after 40 min of milling. The application of a drying step (80 °C for 10 h) favored flowability, in addition to enhancing the tapped density, thus reducing the formation of small pores (< 50 μm), while the density of larger pores (> 100 μm) did not significantly change [82, 95]. The density of the parts produced can be optimized through remelting steps, which eliminate the larger pores; however, remelting steps do not significantly improve the density of AlMgScZr alloy parts built by conventional DLD and using extremely high velocity (extreme high-speed laser material deposition—EHLA) [95]. The addition of ceramic compounds alters the porosity of the final DLD parts. Adding TiC generates a higher density than the addition of SiC, which is attributed to the higher wettability of the former compared with the latter in Al–Mg alloys (4–5 wt. %) [96]. The same authors reported a similar behavior in the DLD processing of AA5024-Sc alloys modified with TiC, where it was observed that the addition of the inoculant delayed the change in powder morphology during the milling process [97].

The DLD processing of Al–W alloys, conventionally used in aerospace and medical applications, has been carried out by in situ mixing of Al powder with 18 wt. % W (2.29 vol. %) in Ref. [98]. The results revealed that the W particles did not fully melt within the aluminum matrix and were deposited in the lower part of the molten layer because of the higher melting point and density than the Al particles [98]. A similar behavior of W particles was reported by Rajamure [99] for Al–W coatings produced by DLD. Approximately 2.25 vol. % W did not melt during DED, while the remaining 0.74 vol. % had Al_4W and $Al_{12}W$ intermetallic phases at temperatures between 400 and 650 °C. Adding W particles increases the hardness of the material [98].

Powder modification

The high reflectivity, thermal conductivity, and low flowability of aluminum alloy powders hinder their L-PBF processing, making it necessary to use high laser power sources to melt the powder and overcome the rapid heat dissipation [33]. Several studies have functionalized the surface of aluminum powders by adding ceramic particles, which present a higher laser absorptivity. Thus, resulting in reduced laser reflectivity during L-PBF [100–102]. Furthermore, the added ceramic particles can act as inoculants, i.e., heterogeneous nucleation sites, leading to a columnar-to-equiaxed microstructure transition and reducing the anisotropy in L-PBF processing [103]. The main ceramic particles used are Al_2O_3, TiC, TiN, TiB_2, SiC, and AlN. The laser reflectivity values of some of these ceramic particles under radiation wavelengths of $\lambda = 1.06$ μm (Nd:YAG fiber laser) and $\lambda = 10.6$ μm (CO_2 laser) are summarized in Table S2, Supplementary Material. The reflectivity of AlSi10Mg alloy is given for comparison.

In the wavelength of $\lambda = 1.06$ μm, the addition of 35 vol.% of TiC to pure aluminum reduced laser reflectivity from 58 to ~ 7.5 % [101], while the addition of 15 wt. % of TiC to the AlSi10Mg alloy powder increased the laser absorptivity by 40 % [102]. Similarly, laser reflectivity decreases from 62 to 25 % when 2 wt. % TiN was added to the AlSi10Mg alloy powder, as shown in Fig. 9(b) [100]. The addition of 15 wt. % of Al_2O_3 to the AlSi10Mg alloy powder increased laser absorptivity by 12 % [104], while the addition of 11.6 wt. % of TiB2 to the AlSi10Mg alloy powder reduced the laser reflectivity by ~ 21 %, and the addition of 2 wt. % nano-SiC to the AlSi7Mg alloy powder reduced laser reflectivity from 31.71 to 23.05 % [104–106].

In addition to the higher laser absorptivity of ceramic particles, the multiple reflections on the powder surface also contribute to an increase in the laser absorptivity of surface-modified powders, as the laser energy is continuously absorbed when the reflected rays interact with other particles instead of simply exiting the powder bed [107]. The occurrence of multiple reflections can explain the increase in the laser absorptivity of modified powders with the addition of ceramics such as Al_2O_3, which presents low laser absorption (Table S2, Supplementary Material) [104]. The laser absorptivity depends on powder composition and surface particle characteristics, such as morphology, size, and surface roughness [107].

As shown by Gu et al. [107], the SiC/AlSi10Mg modified powder presented higher absorptivity than the TiB_2/AlSi10Mg modified powder, both with SiC and TiB_2 particles of the same size (~ 5 μm). The higher absorptivity of the SiC/AlSi10Mg modified powder resulted from fewer interactions of laser rays with the particles compared with the TiB_2 particles because of the reduced power of reflection after every interaction between the laser ray and the SiC/AlSi10Mg powder [107]. Another factor that can influence laser absorptivity is particle morphology since multiple reflections are enhanced on rough and oxidized surfaces [102, 108, 109].

Laser absorptivity also increases with reducing particle size because of the greater penetration of the laser rays into the gaps between particles, strengthening the influence of multiple reflections on the laser absorptivity of the powder [24]. Because of this, ceramic particles are commonly significantly smaller than the matrix powder used in AM, as shown in Table S3 for aluminum alloys and Table S4 for steels (Supplementary Material). The effect of adding TiC particles of 1 and 30 μm sizes on the densification of the AlSi10Mg alloy (powder with an average size of 42 ± 3 μm) produced by L-PBF was analyzed by Zhou et al. [102]. They found an increase in relative density > 99 % for the AlSi10Mg/1 μm TiC powder made using a volumetric energy density of 62.5 J/mm^3, which was lower than the volumetric energy density of 83.3 J/mm^3 necessary to produce the AlSi10Mg alloy with the highest relative density (~ 98.5 %) [102]. In the same study, the relative density of the AlSi10Mg/30 μm TiC samples, produced using

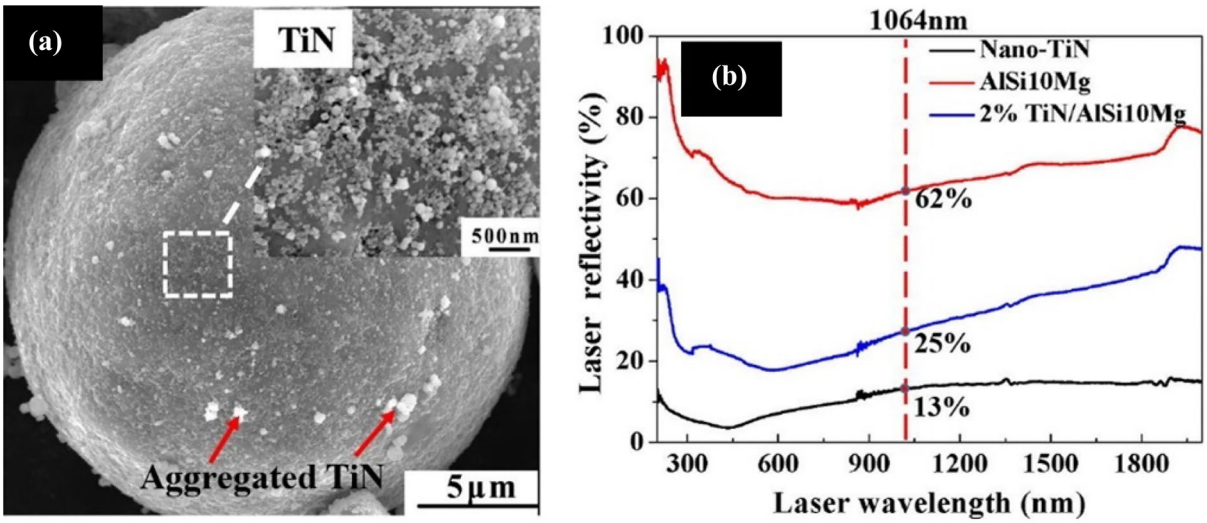

Figure 9: (a) Scanning electron microscopy (SEM) image of the TiN/AlSi10Mg composite powder and (b) reflectivity of the different powders. *Reproduced with permission from Ref.* [100].

different volumetric energy densities, was lower than that of the AlSi10Mg/1 μm TiC combination [102]. The higher melt viscosity resulting from larger TiC particles led to instability of the molten pool, generating a balling effect and higher porosity, consequently reducing the relative density [102]. An increase in relative density from 86.4 to 97.2 % of parts produced by L-PBF was also observed by Chang et al. [110] when smaller SiC particles (D_{50} = 50–5 μm) were mixed with AlSi10Mg powder (D_{50} = 30 μm). The increase in relative density when reducing the SiC particle size resulted from the improvement of the liquid–solid wettability of the smaller particles and the consequent reduction of the molten pool instabilities, balling effect, and porosity [110].

The particles added to aluminum alloy powders can also act as heterogeneous nucleation sites during solidification, leading to a transition from the typical columnar grains observed in the microstructure of L-PBF processed aluminum alloys to a microstructure with equiaxed grains [103, 111]. Columnar grains result from the epitaxial growth due to the high cooling rate and thermal gradient of the L-PBF process and form long intergranular liquid channels, which, together with the thermal stress and solidification shrinkage, can lead to intergranular hot tearing. On the contrary, equiaxed grains can accommodate thermal stress and suppress crack propagation, consequently preventing intergranular hot tearing and improving mechanical properties [103, 112]. Different particles added to aluminum alloy powders for L-PBF were already proven to be efficient in grain refinement, such as ZrH_2 [103], TiN [100], TiC [113], TiB_2 [105], and AlN [114].

Ceramic particles have also been added to steel powders; however, because the laser reflectivity of steels is lower than that of aluminum alloys, ceramic particles are used to increase the strength and stiffness of metal matrix composites (MMCs) produced by L-PBF [115]. The reinforcement of the 316L stainless steel with TiC particles resulted in improved densification and enhanced microhardness and wear performance of parts made by L-PBF [115, 116]. A similar behavior was observed in WC-reinforced Fe-based composites produced by L-PBF with a variation of the process parameters [117]. The addition of TiB_2 reinforcement to the 316L stainless steel powder also resulted in a microstructure of the final parts produced by L-PBF with significant grain refinement, significantly smaller grains compared to pure 316L stainless steel samples attributed to heterogeneous nucleation during solidification [118]. The powder's size, material, and processing conditions are summarized in Table S4 in the Supplementary Material.

In DLD processing, TiC and SiC particles have been added to aluminum alloys, and SiC and WC particles have been added to steels. Adding TiC ceramic particles to the AA5024 aluminum alloy effectively homogenized the powder microstructure, leading to a uniform distribution of grains with different sizes [97]. Similarly, a uniform and dense microstructure was obtained in the 316L stainless steel powder with SiC particles, refining the microstructure and increasing hardness [119].

Different preparation methods have been used to mix the aluminum powder with ceramic particles to avoid agglomeration, which can influence powder morphology and, consequently, laser absorptivity. The most common preparation processes are the direct mixing and ball milling methods. The direct mixing method presents an advantage in the absence of powder plastic deformation, resulting in the ceramic particles' distribution around the matrix powder surface with no morphology modifications [109, 120]. Nano-TiN [100] and nano-SiC [106]

particles were mixed in aluminum alloys using the direct mixing method to maintain the spherical shape of the aluminum powder, as shown in Fig. 10. Nevertheless, the direct mixing method is recommended for low ceramic particle concentrations since the capability of this process to disperse the particles is limited, which can also lead to poor adherence of the ceramic particles to the matrix powder and agglomeration [109, 120].

The matrix powder is repeatedly plastic-deformed and cold-welded during the ball milling method, resulting in the dispersion of the ceramic particles inside the matrix powder [109]. Al_2O_3 [104], TiC [113], TiB_2 [121], SiC [122], and AlN [123] particles have been mixed with aluminum alloys. TiC [116], WC [117], and TiB_2 [118] have been mixed with Fe-based alloys using ball milling, resulting in composite powders with ceramic particles homogeneously distributed and morphology similar to that of the initial matrix powder. The ball milling process parameters should be carefully determined to avoid affecting the morphology of the initial powders, which can influence the packing density and flowability of the composite powder. The mixing time in the ball milling method is shorter than the direct mixing method, and the packing density of the composite powders is typically higher in ball milling [120]. Recently, Wang et al. [121] prepared an AlSi10Mg/2 wt. % TiB_2 powder mixture through ball milling showed that high milling speeds result in large agglomerates with irregular particles and a bimodal PSD. The L-PBF of the powders under such conditions resulted in a balling effect and many small internal pores, which reduced the relative density and mechanical properties compared to the powder mixture prepared using optimized milling speed.

In addition to the mechanical methods to produce composite powders for L-PBF, an in situ reaction method has been used. Nano-TiB_2-reinforced pure aluminum was produced using reactive salts of K_2TiF_6, and KBF_4 added to the molten aluminum metal. The subsequent addition of Mg and Al–Si master alloys, followed by gas atomization, resulted in the nano-TiB_2 decorated AlSi10Mg powder. The method resulted in a powder with spherical morphology and distribution of the nano-TiB_2 particles on the powder surface and along the grain boundaries of the Al–Si matrix powder [105]. Despite the consequent high packing density and flowability, the in situ reaction process is more complex than mechanical methods and can be employed only in a limited number of composite powder systems [120].

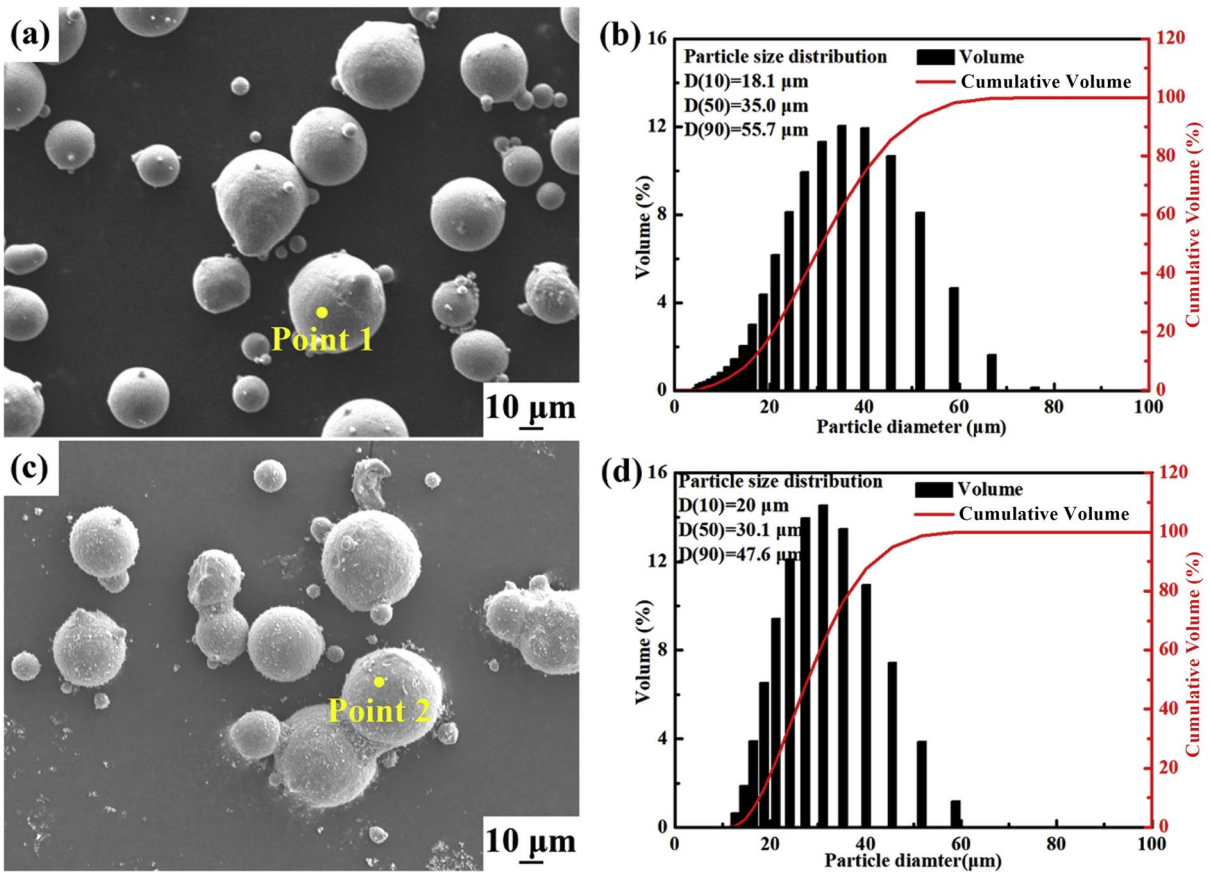

Figure 10: Morphology of (a) AlSi7Mg powder and (c) nano-SiC/AlSi7Mg mixed powders; PSD of (b) AlSi7Mg and (d) nano-SiC/AlSi7Mg powders. . *Reproduced with permission from Ref.* [106].

Two essential characteristics that need to be considered in the preparation of mixed powders are the morphology of the matrix powder and the amount of free (non-attached to the matrix powder) ceramic particles. The spherical morphology, commonly resulting from the gas-atomization process, should be maintained to ensure the high flowability of spherical powders. In addition, the number of free ceramic particles should be minimized to avoid agglomeration and separation in the composite powder, which can lead to microstructural heterogeneity in parts produced by L-PBF. While the non-mechanical method results in well-attached ceramic particles and spherical matrix powders, the dispersion of ceramic particles in the direct mixing method is limited, and the severe plastic deformation of the matrix powder in the ball milling method can result in deviation from the spherical morphology. Therefore, adequate mixing parameters should be used to obtain composite powders with good dispersion of ceramic particles and desired morphology [120].

Graphene [124, 125] and carbon nanotubes (CNTs) [126, 127] have also been mixed with aluminum and aluminum alloy powders for use in L-PBF. Carbon or carbonaceous particles have also effectively increased the laser absorptivity of metal powders with high reflectivity, such as copper alloys [128]. In addition to the ball milling method used to mix these particles, dry coating methods were used to prepare aluminum powders. In an investigation by Zhao et al. [125], the graphene surface was coated with aluminum powder through a chemical reduction in which graphene was added and stirred into an alkyl aluminum solution protected by H_2. The metal coating on the graphene surface increased the wettability between aluminum and graphene, and the composite powder was later ball-milled with AlSi10Mg alloy powder [125]. As a result, a homogeneous distribution of graphene in the AlSi10Mg alloy powder was obtained, which led to a fine microstructure and superior mechanical properties in the AlSi10Mg alloy nanocomposites produced by L-PBF [125]. CNTs were also dispersed onto the surface of the AlSi10Mg alloy powder using an *N*-methyl pyrrolidone reagent [127].

Adding carbon or ceramic particles and coating aluminum powders generates surface roughness, reducing the contact area between the powder surfaces, interparticle adhesion forces, and agglomeration, consequently improving the flowability [129]. Not only the surface roughness but also the surface energy of the particle influences the cohesion/adhesion force and the flowability of the powder, as shown by Jallo et al. [129]. They modified the surface of aluminum powders by dry coating and silane treatment. The dry coating of nano-silica, titania, and carbon and the silane treatment reduced the surface energy and improved the flowability of the aluminum powder [129].

An increase in surface roughness also enhances laser absorptivity, as reported by Bergström et al. [130], especially in metals with high reflectivity, such as aluminum and copper. Chemical etching can be used to obtain rough surfaces with different mechanisms, such as material removal, preferentially from grain boundaries, and increase the surface area and roughness. For example, hydrochloric acid (HCl) [131] and sodium hydroxide (NaOH) [132] solutions have been used to create superhydrophobic surfaces on aluminum substrates, where a rough surface is needed. Adelkhani et al. [133] increased the reflectivity of commercially pure aluminum substrates with decreased surface roughness when the specimens were electropolished in an acidic electrolyte. However, surface functionalization of aluminum powders using these methods has not yet been reported for powder feedstock aimed at AM.

Lastly, a promising method of surface functionalization of metal powders is the controlled oxidation or nitriding treatments to improve laser absorptivity. Arata et al. [134] found an increase in laser absorptivity ($\lambda = 10.6$ μm) with the increase in the thickness of an Al_2O_3 film formed on the surface of pure aluminum powders. Similarly, an increase in the laser absorptivity of pure copper and CuCr1 powders was observed by Jadhav et al. [135, 136] after oxidation and nitriding treatments, respectively. According to the authors, a fine layer of Cu_2O and CuO oxides was formed on the surface of the copper powder during the oxidation treatment, which increased laser absorptivity because of the multiple reflections occurring in the oxide layer [135]. On the contrary, laser absorptivity in the CuCr1 alloy powder increased due to forming a CrN surface layer with high absorptivity [136]. Although these methods have not been used in aluminum powders to be used in AM, as discussed by Jadhav et al. [136], the surface functionalization of metal powders with high reflectivities, such as aluminum alloys, can also be achieved using oxidation and nitriding treatments.

Safety issues in metal powder handling

Although AM can provide significant benefits for industrial applications, it also brings concerns regarding the potential safety of AM production-related activities, e.g., powder handling.

In previous sections, the application of metal powders in AM technologies was covered in detail, and it was clear that fine powder (nanoparticles) could be present despite the size classification of the whole batch before the process [137]. The small particles represent an unnoticeable but serious hazard because they are invisible to the naked eye and can penetrate the human body and cause diseases, for example, cancer [137]. Considering certain conditions, a cloud of fine particles may be prone to fire or explosion, especially aluminum powders exposed to a passivation process after production, as detailed in subsection "Atomization" [137]. Furthermore, it is essential to be careful

with the harmful effects of small particles in the environment [137]. Table S5 in the Supplementary materials details the hazards related to powder handling and how they can be avoided.

In AM processes based on metal powders as feedstock, the material is manipulated in different stages that involve the production, sieving, and handling of the powder and the use and recycling/discarding of the particles during the powder production and building of parts [138]. Although work environments, as well as AM machines, are usually equipped with optimal filtration systems, which minimize contamination by metallic particulates, the health and integrity of the operator may be affected as a result of the manipulation of metal powders in the stages of screening, deposition, cleaning, and elimination of the material [138]. Although the safety suits must protect more vulnerable areas such as the eyes, ears, and nasal passages, protective equipment that favors total body protection is recommended.

The storage of powders is another topic that must be considered for the safety of AM processes. It was suggested that metal powders could increase fire risk because of their high flame temperatures [139]. The risk of ignition and spread of the fire can be affected by several factors, such as the type of metal or alloy, their particle size, the presence of contaminating material, and the disposition of powders since it can favor greater powder preheating and thus a higher rate of spread [140]. To reduce the risk of fire or explosion of powders, it is recommended that they be stored in non-flammable, cooled, and well-ventilated cabinets. Fire extinguishers with special powder against burning metal should be present, as detailed in Table S5, Supplementary material.

Some regulatory agencies and standards should be cited concerning the hazards of powder handling. The US NFPA, NFPA 484, and NFPA 654 standards aim to assist in recognizing possible hazards of combustible solids, including in the form of powder, and preventing the occurrence of fires and dust explosions. The NFPA standard is the most important for people working with metal powders. In Europe, the requirements for commercial products used in potentially explosive atmospheres, such as those containing combustible dust, are provided by the ATEX Directives: ATEX 95 equipment directive 94/9/EC and ATEX 137 workplace directive 99/92/EC, which present the equipment and protective systems and other requirements for the safety and health protection of workers in potentially explosive atmospheres. Additionally, the Australia/New Zealand standard AS/NZS 4745:2004 is a code of recommended practices for handling combustible dust, and the South African national standards SANS 60079-0, SANS 60079-10-2, and SANS 60079-17 present the general requirements for equipment, the classification of areas with combustible dust atmosphere, and a guide for inspection and maintenance of electrical installation in explosive atmospheres, respectively.

Future perspectives

The high reflectivity and thermal conductivity and the low flowability of some powders, as well as the presence of defects (satellites, an oxide layer, porosity, particles with a non-spherical morphology), favor the production of AM parts with low relative density, inferior mechanical performance, and increased production costs due to the need for more significant energy input to ensure the fusion of the metallic powders. Mitigating such issues is a mandatory step to improve the quality of AM-processed parts. In that sense, there are some routes of action to enable the improvement of powders used in L-PBF and DLD. They consider advances in powder production, optimization of powder properties, advanced characterization of powders, and development of new alloys with better intrinsic properties. These routes are discussed in the following.

Beyond the previously highlighted factors, this topic addresses pertinent environmental considerations. Specifically, it explores the recycling of materials designated as "scrap" for the acquisition of suitable powders in additive manufacturing processes. Additionally, it delves into the reuse of metallic powders previously used in additive manufacturing but not integrated into the final product. Both are also discussed.

Advances in powder production and safety

Atomization is the most commonly applied method to produce AM powders. Although some advances have been made concerning equipment design, more development is needed to increase the productivity of powders with the correct characteristics for AM. New types of nozzle geometries should be designed for water and gas atomization to optimize the primary and secondary liquid break-up and to avoid satellites and porosity formation, increasing productivity. Improvements should also be carried out in the design of plasma atomizers to produce powder in a more considerable amount and consequently decrease the costs involved. In addition, process optimization with the assistance of computational simulation and statistical methods, such as the Design of Experiments, would contribute to reducing the number of experiments to optimize the process. One could reach the highest possible yield using an optimized set of processing parameters.

Lastly, alternative routes to produce metal particles could reduce costs and increase yield; for example, ball milling has shown relevant results to be applied to produce metal powder for AM from machining chips.

New designs of AM machines have also been proposed to decrease the operator's contact with powders and avoid issues regarding powder handling. It is essential to increase safety measures in the work environment and within the machines for the operator's safety.

Optimization of powder properties and advanced characterization

Several studies have been conducted on processing metallic materials by L-PBF and DLD. Nevertheless, many studies ignore the importance of the condition of the feedstock during processing. Most studies have focused on the effect of AM-processing parameters, such as laser power or scanning speed, keeping the state of the powders as a "black box," providing only limited data, such as the manufacturer, the fabrication route, and PSD. There is a need to analyze the effect of powders' characteristics during the manufacturing process. A better and more advanced feedstock characterization is needed to understand and optimize AM.

Powders used in AM require a particular average size and particle size distribution. Usually, the users do not try to modify or optimize these properties for the specific alloy and process used. Optimization of size and particle size distribution to obtain optimum flowability and maximum powder bed densification could favor a reduction in the density of defects, increasing the density of the AM parts and improving their mechanical properties.

Additionally, although there are well-established procedures to characterize AM powders, few studies investigated the rheological properties of powders for AM. Such studies are essential to understand the behavior of powder during operation in the machine (i.e., flow inside pipes/nozzles and formation of the powder bed).

Development of AM-friendly alloys

Developing alloys more suitable for additive manufacturing is crucial to improving AM outcomes. However, designing new alloys is costly and requires time and resources. Using computational tools such as computer-aided phase diagram calculations, CALPHAD can assist in predicting the alloys' behavior by estimating thermodynamic and physical properties such as the solidification interval, liquidus temperature, non-equilibrium solidification conditions, and diffusion coefficients, among others. Coupling CALPHAD with machine learning concepts, such as high-performance trials, may accelerate the development of AM-friendly alloys [141]. If physical experimentation is required, laser surface remelting (LSR) allows evaluation of the interaction between the laser and the alloy near the AM conditions, with the benefit of being conducted on bulk samples instead of metallic powder. By avoiding powder use, LSR can quickly give insights into new compositions with a reduced feedstock volume and lower cost [142].

Another promising field is the modification of metal powders. The addition of inoculants, composition modification, and surface modification by chemical processes have presented excellent results in reducing limitations of metal powders, e.g., reflectivity. Powder modification can improve powder properties and broaden the alloy set suitable for laser-based AM processes. Due to the intrinsic characteristics of different metal alloys, their applicability in AM processes becomes complex, requiring several of them to be modified by employing surface treatment or composition variation. In many cases, the literature has focused on the final properties of the parts produced by AM, leaving a gap in the effect that powder modification generates in the properties of the raw material. Powder modification can improve flowability and energy absorption capacity, drastically influencing the powder's processability and applicability in L-PBF and DLD processes.

Finally, using mixed powder with different properties allows for manufacturing functionally graded materials with a gradient of microstructure and chemical composition with length. This strategy is advantageous for improving the metallurgical bond between dissimilar materials and allows tailoring the components' performance by adding high-performance materials in critical locations. In contrast, a low performance, usually a low-cost material, can be used in less-compromising parts of the component [143].

Environmental considerations

Climate change is increasingly being acknowledged by society as a phenomenon of growing intensity and severity, culminating in catastrophes and raising concerns about a menacing future [144]. According to the United States Environmental Protection Agency, in 2019, the industrial sector contributed 22.9 % to the total gas emissions, with particular emphasis on the steel, iron, and metallurgical coke production industries, accounting for 41.3 % of industrial emissions [144]. Among the primary opportunities for emission reduction in the industry, recycling practices stand out [144].

De Souza and Pacca [145] highlighted the possibility of recycling iron and steel scraps to produce new raw materials, generating new products, and reducing waste, CO_2 emissions, and mineral exploitation. In this context, De Araújo et al. [146] evaluated an in situ Al-matrix quasicrystalline Al–Fe–Cr–Ti composite powder produced using recycled aluminum cans as the base material, which were processed by L-PBF providing an effective way to fabricate tailored Al–Fe–Cr–Ti composites' parts by L-PBF.

Another way to reduce waste, CO_2 emissions, and mineral exploitation could be the reuse of powder since during the AM process only a fraction of the powder is fused and solidified as a part [147]. However, the properties of the "non-used" powder may exhibit variances compared to those of the virgin material following exposure to the AM environment [147]. The reuse of

powder has the potential to adversely affect the properties of the final components [147]. He et al. [148] conducted a comparative analysis of virgin and reused powder over six iterations to evaluate the mechanical properties of Hastelloy X alloy manufactured through L-PBF. As a result, a 20.8 % reduction in the ductility of the L-PBF Hastelloy X, fabricated using recycled powder, was observed [148]. On the other hand, Delacroix et al. [147] did not detect noteworthy distinctions in the microhardness and tensile properties of L-PBF components manufactured using virgin and reused (15 times) 316L powders. Nevertheless, a reduction in part density was noted with powder reuse, and the microstructure exhibited a greater abundance of finer grains across successive reuse cycles [147]. Enhancing our comprehension of the influence of powder reuse on both the powder quality and the printed components is imperative.

Conclusions

Applying additive manufacturing processes has been greatly welcomed in producing metallic components. Although several AM processes, laser powder bed fusion, and direct laser deposition techniques stand out in metal processing. The characteristics of the metal powders used as feedstock in these processes influence the building parameters, the quality of the built parts, and their mechanical and physical properties.

Aluminum-based alloys and steels are highly demanded in various industrial sectors; therefore, their application in AM processes has been intensively investigated over the last 15 years. The built parts' quality, physical characteristics, and mechanical properties are linked to different process variables, including the feedstock powders' physical and rheological properties. L-PBF generally requires a reasonably small particle size, usually 15–45 μm, whereas the range varies between 50 and 200 μm in DLD processing. Such difference in powder size influences several properties of AM-built parts, such as surface roughness.

Different methods can be employed to produce metal powders. Among them, chemical (chemical reduction or decomposition of compounds), mechanical (ball or vortex milling processes), and physical (electrolytic and atomization processes) methods stand out. Atomization is the most used method to produce powders aimed at AM processes. Atomized powders usually have an optimal particle size distribution and adequate morphology, water atomization being an exception when it comes to particle morphology. Nonetheless, defects such as surface oxide layers, porosity, and satellite particles can occur. Gas atomization has shown promising results for highly reactive materials like aluminum.

Metal powders should present optimal flowability and PSD to ensure maximum powder layer density (in the case of L-PBF), influencing the AM parts' density. Several methods are used to determine the PSD of powders, among which sieving, laser light diffraction, and image analysis stand out. The application of automated systems such as dynamic image analysis has been well accepted in determining the PSD and morphology of metallic particles because of their greater accuracy, versatility, speed of analysis, and ease of use compared with other methods.

Laser absorptivity is an intrinsic property of the material and directly influences its processability in AM. Aluminum alloys present high reflectivity, reaching 91 % when an Nd:YAG laser source is used. In contrast, AISI 316L stainless steel gives a laser reflectivity of up to 41 % using the same source. The high reflectivity of aluminum reduces the amount of absorbed heat supplied by the laser source, requiring more significant energy input to ensure powder fusion. The higher energy input reflects increased processing costs and favors the formation of defects such as porosity.

Modifying metal powders' surfaces has aroused great interest in reducing shortcomings such as high reflectivity, high thermal conductivity, and low flowability. Adding new alloying elements and incorporating inoculating agents (mainly ceramic particles) into metal powders favor more outstanding AM processability. In addition, the decrease in the surface energy and interparticle adhesion force and the modification of powder morphology with surface functionalization through chemical etching, coating, oxidation, and nitriding treatments have a great potential to increase the processability of aluminum powders and can open a large field for investigations in AM processing.

Finally, the control during powder production, handling, and storage must be carefully considered to ensure the integrity and health of the operator and the surrounding environment. Because of their size and high reactivity, metal powders can cause respiratory and skin problems, for which the operator must be protected to avoid direct contact with the material as much as possible. Likewise, poor storage of powders can lead to their reaction to the surrounding environment, causing fires or explosions. Although current machines have excellent filtration systems that can mitigate several of these risks, they increase during powders' transport, cleaning, recycling, and storage stages before and after their processing by AM.

Acknowledgments

This study was supported in part by the *Coordenação de Aperfeiçoamento de Pessoal de Nível Superior* (CAPES) – Brazil – Finance code 001. The authors are grateful to the São Paulo Research Foundation (FAPESP) for the Grants 2017/27031-4, 2020/01452-6, 2020/08145-1, 2020/09544-7, 2020/01426-5, 2019/01829-5, and 2021/12056-7.

Author contributions

LETM: formal analysis, and writing—original draft. VEP: formal analysis, and writing—original draft. BFB: formal analysis, and writing—original draft. NR-A: formal analysis, and writing—original draft. GF: formal analysis, and writing—original draft. AFA: writing—review & editing, and validation. PG: writing—review & editing, validation, resources, funding acquisition, and supervision.

Data availability

Data sets generated during the current study are available from the corresponding author upon reasonable request.

Declarations

Competing interests The authors declare that they have no known competing financial interests or personal relationships that could have appeared to influence the work reported in this paper.

Supplementary Information

The online version contains supplementary material available at https://doi.org/10.1557/s43578-023-01271-8.

Open Access

References

1. T. Debroy, H.L. Wei, J.S. Zuback, T. Mukherjee, J.W. Elmer, J.O. Milewski, A.M. Beese, A. Wilson-heid, A. De, W. Zhang, Additive manufacturing of metallic components—process, structure and properties. Prog. Mater. Sci. **92**, 112–224 (2018). https://doi.org/10.1016/j.pmatsci.2017.10.001
2. S.M. Thompson, L. Bian, N. Shamsaei, A. Yadollahi, An overview of direct laser deposition for additive manufacturing; part I: transport phenomena, modeling and diagnostics. Addit. Manuf. **8**, 36–62 (2015). https://doi.org/10.1016/j.addma.2015.07.001
3. B.H. Jared, M.A. Aguilo, L.L. Beghini, B.L. Boyce, B.W. Clark, A. Cook, B.J. Kaehr, J. Robbins, Additive manufacturing: toward holistic design. Scr. Mater. **135**, 141–147 (2017). https://doi.org/10.1016/j.scriptamat.2017.02.029
4. S. Cooke, K. Ahmadi, S. Willerth, R. Herring, Metal additive manufacturing: technology, metallurgy and modeling. J. Manuf. Process. **57**, 978–1003 (2020). https://doi.org/10.1016/j.jmapro.2020.07.025
5. S.A. Khairallah, A.T. Anderson, A. Rubenchik, W.E. King, Laser powder-bed fusion additive manufacturing: physics of complex melt flow and formation mechanisms of pores, spatter, and denudation zones. Acta Mater. **108**, 36–45 (2016). https://doi.org/10.1016/j.actamat.2016.02.014
6. A.T. Sutton, C.S. Kriewall, M.C. Leu, J.W. Newkirk, Powder characterisation techniques and effects of powder characteristics on part properties in powder-bed fusion processes. Virtual Phys. Prototyp. **12**, 3–29 (2017). https://doi.org/10.1080/17452759.2016.1250605
7. S. Vock, B. Klöden, A. Kirchner, T. Weißgärber, B. Kieback, Powders for powder bed fusion: a review. Progr. Addit. Manuf. **4**, 383–397 (2019). https://doi.org/10.1007/s40964-019-00078-6
8. S. Pasebani, M. Ghayoor, S. Badwe, H. Irrinki, S.V. Atre, Effects of atomizing media and post processing on mechanical properties of 17-4 PH stainless steel manufactured via selective laser melting. Addit. Manuf. **22**, 127–137 (2018). https://doi.org/10.1016/j.addma.2018.05.011
9. L.E.T. Mathias, A.F. Andreoli, P. Gargarella, Gas atomization of A2 tool steel: effect of process parameters on powders' physical properties. J. Alloys Compd. (2023). https://doi.org/10.1016/j.jallcom.2023.170696
10. H. Lubanska, Correlation of spray ring data for gas atomization of liquid metals. J. Met. **22**, 45–49 (1970). https://doi.org/10.1007/bf03355938
11. G. Varga, J. Kovács, Z. Szalai, C. Cserháti, G. Újvári, Granulometric characterization of paleosols in loess series by automated static image analysis. Sediment. Geol. **370**, 1–14 (2018). https://doi.org/10.1016/j.sedgeo.2018.04.001
12. P.K.D.S. Bomfim, F.G. Coury, P. Wang, P. Gargarella, Characterization of AlCoCrFeNi high entropy alloy gas atomized powder. Mater. Res. (2022). https://doi.org/10.1590/1980-5373-MR-2021-0120
13. F. Chu, K. Zhang, H. Shen, M. Liu, W. Huang, X. Zhang, E. Liang, Z. Zhou, L. Lei, J. Hou, A. Huang, Influence of satellite and agglomeration of powder on the processability of AlSi10Mg powder in laser powder bed fusion. J. Market. Res. **11**, 2059–2073 (2021). https://doi.org/10.1016/j.jmrt.2021.02.015

14. X. Gang Li, Q. Zhu, S. Shu, J. Zhong Fan, S. Ming Zhang, Fine spherical powder production during gas atomization of pressurized melts through melt nozzles with a small inner diameter. Powder Technol. **356**, 759–768 (2019). https://doi.org/10.1016/j.powtec.2019.09.023
15. L. Marchetti, C. Hulme-Smith, Flowability of steel and tool steel powders: a comparison between testing methods. Powder Technol. **384**, 402–413 (2021). https://doi.org/10.1016/j.powtec.2021.01.074
16. A.B. Spierings, M. Voegtlin, T. Bauer, K. Wegener, Powder flowability characterisation methodology for powder-bed-based metal additive manufacturing. Progr. Addit. Manuf. **1**, 9–20 (2016). https://doi.org/10.1007/s40964-015-0001-4
17. N.K. Tolochko, T. Laoui, Y.V. Khlopkov, S.E. Mozzharov, V.I. Titov, M.B. Ignatiev, Absorptance of powder materials suitable for laser sintering. Rapid Prototyp. J. **6**, 155–160 (2000). https://doi.org/10.1108/13552540010337029
18. D.D. Gu, W. Meiners, K. Wissenbach, R. Poprawe, Laser additive manufacturing of metallic components: materials, processes and mechanisms. Int. Mater. Rev. **57**, 133–164 (2012). https://doi.org/10.1179/1743280411Y.0000000014
19. E. Louvis, P. Fox, C.J. Sutcliffe, Selective laser melting of aluminium components. J. Mater. Process. Technol. **211**, 275–284 (2011). https://doi.org/10.1016/j.jmatprotec.2010.09.019
20. S.D. Jadhav, L.R. Goossens, Y. Kinds, B. Van Hooreweder, K. Vanmeensel, Laser-based powder bed fusion additive manufacturing of pure copper. Addit. Manuf. **42**, 101990 (2021). https://doi.org/10.1016/j.addma.2021.101990
21. D. Schreuder, *Outdoor Lighting: Physics, Vision and Perception* (Springer, Netherlands, Dordrecht, 2008). https://doi.org/10.1007/978-1-4020-8602-1
22. G.S. Brady, H.R. Clauser, J.A. Vaccari, *Materials Handbook*, 15th edn. (McGraw-Hill, New York, 2002)
23. A.B. Spierings, N. Herres, G. Levy, Influence of the particle size distribution on surface quality and mechanical properties in AM steel parts. Rapid Prototyp. J. **17**, 195–202 (2011). https://doi.org/10.1108/13552541111124770
24. Y. Yang, D. Gu, D. Dai, C. Ma, Laser energy absorption behavior of powder particles using ray tracing method during selective laser melting additive manufacturing of aluminum alloy. Mater. Des. **143**, 12–19 (2018). https://doi.org/10.1016/j.matdes.2018.01.043
25. M.A. Balbaa, A. Ghasemi, E. Fereiduni, M.A. Elbestawi, S.D. Jadhav, J.-P. Kruth, Role of powder particle size on laser powder bed fusion processability of AlSi10Mg alloy. Addit. Manuf. **37**, 101630 (2021). https://doi.org/10.1016/j.addma.2020.101630
26. J.A. Muñiz-lerma, A. Nommeots-nomm, K.E. Waters, M. Brochu, A comprehensive approach to powder feedstock characterization for powder bed fusion additive manufacturing: a case study on AlSi7Mg. Materials (2018). https://doi.org/10.3390/ma11122386
27. A. Hatem, C. Schulz, T. Schlaefer, J.T. Boobhun, N. Stanford, C. Hall, Influence of laser absorption by water- and gas-atomised powder feedstock on laser metal deposition of AISI 431 stainless steel. Addit. Manuf. **47**, 102242 (2021). https://doi.org/10.1016/j.addma.2021.102242
28. O.D. Neikov, S.S. Naboychenko, G. Dowson, *Handbook of Non-ferrous Metal Powders Technologies and Applications*, 1st edn. (Elsevier, Amsterdam, 2009)
29. G.S. Upadhyaya, *Powder Metallurgy Technology*, 1st edn. (Cambridge International Science Publishing, Cambridge, 2002)
30. J. Dawes, R. Bowerman, R. Trepleton, Introduction to the additive manufacturing powder metallurgy supply chain. Johnson Matthey Technol. Rev. **59**, 243–256 (2015). https://doi.org/10.1595/205651315X688686
31. L. Cordova, T. Bor, M. de Smit, M. Campos, T. Tinga, Measuring the spreadability of pre-treated and moisturized powders for laser powder bed fusion. Addit. Manuf. **32**, 101082 (2020). https://doi.org/10.1016/j.addma.2020.101082
32. R. Baitimerov, P. Lykov, D. Zherebtsov, L. Radionova, A. Shultc, K.G. Prashanth, Influence of powder characteristics on processability of AlSi12 alloy fabricated by selective laser melting. Materials **11**, 1–14 (2018). https://doi.org/10.3390/ma11050742
33. D. Herzog, V. Seyda, E. Wycisk, C. Emmelmann, Additive manufacturing of metals. Acta Mater. **117**, 371–392 (2016). https://doi.org/10.1016/j.actamat.2016.07.019
34. K. Abd-Elghany, D.L. Bourell, Property evaluation of 304L stainless steel fabricated by selective laser melting. Rapid Prototyp. J. **18**, 420–428 (2012). https://doi.org/10.1108/13552541211250418
35. I.E. Anderson, E.M.H. White, R. Dehoff, Feedstock powder processing research needs for additive manufacturing development. Curr. Opin. Solid State Mater. Sci. **22**, 8–15 (2018). https://doi.org/10.1016/j.cossms.2018.01.002
36. D. Riabov, E. Hryha, M. Rashidi, S. Bengtsson, L. Nyborg, Effect of atomization on surface oxide composition in 316L stainless steel powders for additive manufacturing. Surf. Interface Anal. **52**, 694–706 (2020). https://doi.org/10.1002/sia.6846
37. C. Degueldre, S. O'Prey, W. Francioni, An in-line diffuse reflection spectroscopy study of the oxidation of stainless steel under boiling water reactor conditions. Corros. Sci. **38**, 1763–1782 (1996). https://doi.org/10.1016/S0010-938X(96)00078-9
38. A. Popovich, V. Sufiiarov, in *Metal Powder Additive Manufacturing*, ed. by I. V. Shishkovsky. New Trends in 3D Printing (InTech, 2016), p. 227. https://doi.org/10.1007/s11837-015-1321-z
39. K. Kassym, A. Perveen, Atomization processes of metal powders for 3D printing. Mater. Today Proc. **26**, 1727–1733 (2020). https://doi.org/10.1016/j.matpr.2020.02.364
40. C. Schade, J.J. Dunkley, Atomization. Powder Metall. (2015). https://doi.org/10.31399/asm.hb.v07.a0006084

41. G. Matsagopane, E.O. Olakanmi, A. Botes, S. Kutua, Conceptual design framework for setting up aluminum alloy powder production system for selective laser melting (SLM) process. JOM **71**, 1843–1860 (2019). https://doi.org/10.1007/s11837-019-03431-w
42. M. Entezarian, F. Allaire, P. Tsantrizos, R.A.L. Drew, Plasma atomization: a new process for the production of fine, spherical powders. JOM **48**, 53–55 (1996). https://doi.org/10.1007/BF03222969
43. T. Fedina, J. Sundqvist, J. Powell, A.F.H. Kaplan, A comparative study of water and gas atomized low alloy steel powders for additive manufacturing. Addit. Manuf. **36**, 101675 (2020). https://doi.org/10.1016/j.addma.2020.101675
44. J.J. Dunkley, Metal powder atomisation methods for modern manufacturing. Johnson Matthey Technol. Rev. **63**, 226–232 (2019). https://doi.org/10.1595/205651319x15583434137356
45. S. Dietrich, M. Wunderer, A. Huissel, M.F. Zaeh, A new approach for a flexible powder production for additive manufacturing. Procedia Manuf. **6**, 88–95 (2016). https://doi.org/10.1016/j.promfg.2016.11.012
46. A.A. Gromov, A.P. Il'In, U. Foerter-Barth, U. Teipel, Effect of the passivating coating type, particle size, and storage time on oxidation and nitridation of aluminum powders. Combust. Explos. Shock Waves **42**, 177–184 (2006). https://doi.org/10.1007/s10573-006-0036-4
47. K. Riener, S. Oswald, M. Winkler, G.J. Leichtfried, Influence of storage conditions and reconditioning of AlSi10Mg powder on the quality of parts produced by laser powder bed fusion (LPBF). Addit. Manuf. **39**, 101896 (2021). https://doi.org/10.1016/j.addma.2021.101896
48. B. Zheng, Y. Lin, Y. Zhou, E.J. Lavernia, Gas atomization of amorphous aluminum: Part I. Thermal behavior calculations. Metall. Mater. Trans. B **40**, 768–778 (2009). https://doi.org/10.1007/s11663-009-9276-5
49. J. Ting, I.E. Anderson, A computational fluid dynamics (CFD) investigation of the wake closure phenomenon. Mater. Sci. Eng. A **379**, 264–276 (2004). https://doi.org/10.1016/j.msea.2004.02.065
50. R. Ünal, Improvements to close coupled gas atomisation nozzle for fine powder production. Powder Metall. **50**, 66–71 (2007). https://doi.org/10.1179/174329007X164899
51. A. Lawley, Atomization of specialty alloy powders. J. Met. **33**, 13–18 (1981). https://doi.org/10.1007/bf03354395
52. A. Ünal, Effect of processing variables on particle size in gas atomization of rapidly solidified aluminium powders. Mater. Sci. Technol. **3**, 1029–1039 (1987)
53. C. Dungkratok, N. Srisukhumbowornchai, K. Fakpan, M. Morakotjinda, N. Tosangthum, O. Coovattanachai, R. Krataitong, A. Daraphan, B. Vetayanugul, R. Tongsri, Analysis of tin powder production using a pilot gas atomiser, in *19th Conference of Mechanical Engineering Network of Thailand* (2005), pp. 1–5
54. E. Urionabarrenetxea, A. Avello, A. Rivas, J.M. Martín, Experimental study of the influence of operational and geometric variables on the powders produced by close-coupled gas atomisation. Mater. Des. **199**, 109441 (2021). https://doi.org/10.1016/j.matdes.2020.109441
55. B. Zheng, Y. Lin, Y. Zhou, E.J. Lavernia, Gas atomization of amorphous aluminum powder: Part II. Experimental investigation. Metall. Mater. Trans. B **40**, 995–1004 (2009). https://doi.org/10.1007/s11663-009-9277-4
56. C. Feng Gao, Z. Yu Xiao, H. Ping Zou, Z. Qiang Liu, J. Chen, S. Kui Li, D. Tong Zhang, Characterization of spherical AlSi10Mg powder produced by double-nozzle gas atomization using different parameters. Trans. Nonferrous Met. Soc. China (Engl. Ed.) **29**, 374–384 (2019). https://doi.org/10.1016/S1003-6326(19)64947-2
57. A. Allimant, M.P. Planche, Y. Bailly, L. Dembinski, C. Coddet, Progress in gas atomization of liquid metals by means of a De Laval nozzle. Powder Technol. **190**, 79–83 (2009). https://doi.org/10.1016/j.powtec.2008.04.071
58. A. Lawley, *Atomization: The Production of Metal Powders*, 1st edn. (Metal Powder Industries Federation, Princeton, 1992)
59. A. Ünal, Production of rapidly solidified aluminium alloy powders by gas atomisation and their applications. Powder Metall. **33**, 53–64 (1990). https://doi.org/10.1179/pom.1990.33.1.53
60. F.C. da Silva, M.L. de Lima, G.F. Colombo, Evaluation of a mathematical model based on Lubanska equation to predict particle size for close-coupled gas atomization of 316L stainless steel. Mater. Res. (2022). https://doi.org/10.1590/1980-5373-mr-2021-0364
61. S. Dhiman, R.S. Joshi, S. Singh, S.S. Gill, H. Singh, R. Kumar, V. Kumar, Recycling of Ti6Al4V machining swarf into additive manufacturing feedstock powder to realise sustainable recycling goals. J. Clean. Prod. **348**, 131342 (2022). https://doi.org/10.1016/j.jclepro.2022.131342
62. B. Fullenwider, P. Kiani, J.M. Schoenung, K. Ma, Two-stage ball milling of recycled machining chips to create an alternative feedstock powder for metal additive manufacturing. Powder Technol. **342**, 562–571 (2019). https://doi.org/10.1016/j.powtec.2018.10.023
63. A. Lawley, High-Energy Ball Milling: Mechanochemical Processing of Nanopowders, 1st edn. (Woodhead Publishing, 2010)
64. C. Suryanarayana, Mechanical alloying and milling. Prog. Mater. Sci. **46**, 1–184 (2001)
65. R.M. Leal Neto, C.J. Rocha, E. Urano de Carvalho, H.G. Riella, M. Durazzo, Investigation of powdering ductile gamma U-10wt%Mo alloy for dispersion fuels. J. Nucl. Mater. **445**, 218–223 (2014). https://doi.org/10.1016/j.jnucmat.2013.11.014
66. S. Dhiman, R.S. Joshi, S. Singh, S.S. Gill, H. Singh, R. Kumar, V. Kumar, A framework for effective and clean conversion of

machining waste into metal powder feedstock for additive manufacturing. Clean. Eng. Technol. **4**, 100151 (2021)
67. C. de Sales Pereira Mendonça, A.F. Oliveira, L.A. Oliveira, M.R. da Silva, M. de Lourdes Noronha Motta Melo, G. Silva, Structural and magnetic properties of duplex stainless steel (UNS S31803) powders obtained by high energy milling of chips with additions of NbC. Mater. Res. (2018). https://doi.org/10.1590/1980-5373-mr-2017-0717
68. C. Zhong, J. Chen, S. Linnenbrink, A. Gasser, S. Sui, R. Poprawe, A comparative study of Inconel 718 formed by high deposition rate laser metal deposition with GA powder and PREP powder. Mater. Des. **107**, 386–392 (2016). https://doi.org/10.1016/j.matdes.2016.06.037
69. P. Sun, Z.Z. Fang, Y. Xia, Y. Zhang, C. Zhou, A novel method for production of spherical Ti-6Al-4V powder for additive manufacturing. Powder Technol. **301**, 331–335 (2016). https://doi.org/10.1016/j.powtec.2016.06.022
70. Z.Z. Fang, J.D. Paramore, P. Sun, K.S.R. Chandran, Y. Zhang, Y. Xia, F. Cao, M. Koopman, M. Free, Powder metallurgy of titanium—past, present, and future. Int. Mater. Rev. **63**, 407–459 (2018). https://doi.org/10.1080/09506608.2017.1366003
71. A. Simchi, The role of particle size on the laser sintering of iron powder. Metall. Mater. Trans. **35B**, 937–948 (2004)
72. B. Liu, R. Wildman, C. Tuck, I. Ashcroft, R. Hague, *Investigation the Effect of Particle Size Distribution on Processing Parameters Optimization in Selective Laser Melting Process* (Additive Manufacturing Research Group, Loughborough University, Loughborough, 2011), pp.227–238
73. I. Tolosa, F. Garciandía, F. Zubiri, F. Zapirain, A. Esnaola, Study of mechanical properties of AISI 316 stainless steel processed by "selective laser melting", following different manufacturing strategies. Int. J. Adv. Manuf. Technol. **51**, 639–647 (2010). https://doi.org/10.1007/s00170-010-2631-5
74. K. Riener, N. Albrecht, S. Ziegelmeier, R. Ramakrishnan, L. Haferkamp, A.B. Spierings, G.J. Leichtfried, Influence of particle size distribution and morphology on the properties of the powder feedstock as well as of AlSi10Mg parts produced by laser powder bed fusion (LPBF). Addit. Manuf. **34**, 101286 (2020). https://doi.org/10.1016/j.addma.2020.101286
75. M. Abdelwahed, R. Casati, S. Bengtsson, A. Larsson, M. Riccio, M. Vedani, Effects of powder atomisation on microstructural and mechanical behaviour of L-PBF processed steels. Metals (Basel) **10**, 1–21 (2020). https://doi.org/10.3390/met10111474
76. S.-S. Park, E.S. Kim, Jamming probability of granular flow in 3D hopper with shallow columns: DEM simulations. Granul. Matter **22**, 77 (2020). https://doi.org/10.1007/s10035-020-01050-w
77. T.B. Sercombe, X. Li, Selective laser melting of aluminium and aluminium metal matrix composites: review. Mater. Technol. **31**, 77–85 (2016). https://doi.org/10.1179/1753555715Y.0000000078
78. T. Qi, H. Zhu, H. Zhang, J. Yin, L. Ke, X. Zeng, Selective laser melting of Al7050 powder: melting mode transition and comparison of the characteristics between the keyhole and conduction mode. Mater. Des. **135**, 257–266 (2017). https://doi.org/10.1016/j.matdes.2017.09.014
79. N. Kaufmann, M. Imran, T.M. Wischeropp, C. Emmelmann, S. Siddique, F. Walther, Influence of process parameters on the quality of aluminium alloy EN AW 7075 using selective laser melting (SLM). Phys. Procedia **83**, 918–926 (2016). https://doi.org/10.1016/j.phpro.2016.08.096
80. M.L. Montero Sistiaga, R. Mertens, B. Vrancken, X. Wang, B. Van Hooreweder, J.P. Kruth, J. Van Humbeeck, Changing the alloy composition of Al7075 for better processability by selective laser melting. J. Mater. Process. Technol. **238**, 437–445 (2016). https://doi.org/10.1016/j.jmatprotec.2016.08.003
81. P. Wang, Al-3.5Cu-1.5Mg-1Si alloy and related materials produced by selective laser melting. Laser Tech. (2018). https://doi.org/10.1002/latj.201290018
82. X.P. Li, K.M. O'Donnell, T.B. Sercombe, Selective laser melting of Al-12Si alloy: enhanced densification via powder drying. Addit. Manuf. **10**, 10–14 (2016). https://doi.org/10.1016/j.addma.2016.01.003
83. J.W. Xie, P. Fox, W. O'Neill, C.J. Sutcliffe, Effect of direct laser re-melting processing parameters and scanning strategies on the densification of tool steels. J. Mater. Process. Technol. **170**, 516–523 (2005). https://doi.org/10.1016/j.jmatprotec.2005.05.055
84. K.A. Mumtaz, P. Erasenthiran, N. Hopkinson, High density selective laser melting of Waspaloy®. J. Mater. Process. Technol. **195**, 77–87 (2008). https://doi.org/10.1016/j.jmatprotec.2007.04.117
85. S. Leuders, M. Thöne, A. Riemer, T. Niendorf, T. Tröster, H.A. Richard, H.J. Maier, On the mechanical behaviour of titanium alloy TiAl6V4 manufactured by selective laser melting: fatigue resistance and crack growth performance. Int. J. Fatigue **48**, 300–307 (2013). https://doi.org/10.1016/j.ijfatigue.2012.11.011
86. K.L. Terrassa, J.C. Haley, B.E. MacDonald, J.M. Schoenung, Reuse of powder feedstock for directed energy deposition. Powder Technol. **338**, 819–829 (2018). https://doi.org/10.1016/j.powtec.2018.07.065
87. S. Li, B. Chen, C. Tan, X. Song, Study on recyclability of 316L stainless steel powder by using laser directed energy deposition. J. Mater. Eng. Perform. (2021). https://doi.org/10.1007/s11665-021-06150-z
88. A.J. Pinkerton, L. Li, Direct additive laser manufacturing using gas- and water-atomised H13 tool steel powders. Int. J. Adv. Manuf. Technol. **25**, 471–479 (2005). https://doi.org/10.1007/s00170-003-1844-2
89. M.A. Jackson, A. Kim, J.A. Manders, D.J. Thoma, F.E. Pfefferkorn, Production of mechanically-generated 316L stainless steel feedstock and its performance in directed energy

deposition processing as compared to gas-atomized powder. CIRP J. Manuf. Sci. Technol. **31**, 233–243 (2020). https://doi.org/10.1016/j.cirpj.2020.05.014

90. A. Da Silva, J. Volpp, A.F.H. Kaplan, The effects of laser irradiation on an aluminium powder stream in directed energy deposition. Addit. Manuf. **41**, 101968 (2021). https://doi.org/10.1016/j.addma.2021.101968
91. M. Leitner, T. Leitner, A. Schmon, K. Aziz, G. Pottlacher, Thermophysical properties of liquid aluminum. Metall. Mater. Trans. A **48**, 3036–3045 (2017). https://doi.org/10.1007/s11661-017-4053-6
92. A.L. Klein, W. Bouwhuis, C.W. Visser, H. Lhuissier, C. Sun, J.H. Snoeijer, E. Villermaux, D. Lohse, H. Gelderblom, Drop shaping by laser-pulse impact. Phys. Rev. Appl. **3**, 44018 (2015). https://doi.org/10.1103/PhysRevApplied.3.044018
93. H. Tan, Y. Fang, C. Zhong, Z. Yuan, W. Fan, Z. Li, J. Chen, X. Lin, Investigation of heating behavior of laser beam on powder stream in directed energy deposition. Surf. Coat. Technol. **397**, 126061 (2020). https://doi.org/10.1016/j.surfcoat.2020.126061
94. I. Tabernero, A. Lamikiz, S. Martínez, E. Ukar, L.N. López de Lacalle, Modelling of energy attenuation due to powder flow-laser beam interaction during laser cladding process. J. Mater. Process. Technol. **212**, 516–522 (2012). https://doi.org/10.1016/j.jmatprotec.2011.10.019
95. T. Zhao, Y. Wang, T. Xu, M. Bakir, W. Cai, M. Wang, M. Dahmen, Q. Zheng, X. Wei, C. Hong, C. Zhong, P. Albus, T. Schopphoven, A. Gasser, C.L. Häfner, Some factors affecting porosity in directed energy deposition of AlMgScZr-alloys. Opt. Laser Technol. **143**, 107337 (2021). https://doi.org/10.1016/j.optlastec.2021.107337
96. A. Contreras, E. Bedolla, R. Pérez, Interfacial phenomena in wettability of TiC by Al–Mg alloys. Acta Mater. **52**, 985–994 (2004). https://doi.org/10.1016/j.actamat.2003.10.034
97. T. Zhao, M. Dahmen, W. Cai, M. Alkhayat, J. Schaible, P. Albus, C. Zhong, C. Hong, T. Biermann, H. Zhang, D. Gu, A. Weisheit, A. Gasser, J.H. Schleifenbaum, Laser metal deposition for additive manufacturing of AA5024 and nanoparticulate TiC modified AA5024 alloy composites prepared with balling milling process. Opt. Laser Technol. **131**, 106438 (2020). https://doi.org/10.1016/j.optlastec.2020.106438
98. A. Ramakrishnan, G.P. Dinda, Microstructural control of an Al–W aluminum matrix composite during direct laser metal deposition. J. Alloys Compd. **813**, 152208 (2020). https://doi.org/10.1016/j.jallcom.2019.152208
99. R.S. Rajamure, H.D. Vora, S.G. Srinivasan, N.B. Dahotre, Laser alloyed Al-W coatings on aluminum for enhanced corrosion resistance. Appl. Surf. Sci. **328**, 205–214 (2015). https://doi.org/10.1016/j.apsusc.2014.12.037
100. C. Gao, Z. Xiao, Z. Liu, Q. Zhu, W. Zhang, Selective laser melting of nano-TiN modified AlSi10Mg composite powder with low laser reflectivity. Mater. Lett. **236**, 362–365 (2019). https://doi.org/10.1016/j.matlet.2018.10.126
101. T.C. Lin, C. Cao, M. Sokoluk, L. Jiang, X. Wang, J.M. Schoenung, E.J. Lavernia, X. Li, Aluminum with dispersed nanoparticles by laser additive manufacturing. Nat. Commun. (2019). https://doi.org/10.1038/s41467-019-12047-2
102. S.Y. Zhou, Z.Y. Wang, Y. Su, H. Wang, G. Liu, T.T. Song, M. Yan, Effects of micron/submicron TiC on additively manufactured AlSi10Mg: a comprehensive study from computer simulation to mechanical and microstructural analysis. JOM (2020). https://doi.org/10.1007/s11837-019-03984-w
103. J.H. Martin, B.D. Yahata, J.M. Hundley, J.A. Mayer, T.A. Schaedler, T.M. Pollock, 3D printing of high-strength aluminium alloys. Nature **549**, 365–369 (2017). https://doi.org/10.1038/nature23894
104. H. Liao, H. Zhu, G. Xue, X. Zeng, Alumina loss mechanism of Al_2O_3-AlSi10Mg composites during selective laser melting. J. Alloys Compd. **785**, 286–295 (2019). https://doi.org/10.1016/j.jallcom.2019.01.116
105. X.P. Li, G. Ji, Z. Chen, A. Addad, Y. Wu, H.W. Wang, J. Vleugels, J. Van Humbeeck, J.P. Kruth, Selective laser melting of nano-TiB2 decorated AlSi10Mg alloy with high fracture strength and ductility. Acta Mater. **129**, 183–193 (2017). https://doi.org/10.1016/j.actamat.2017.02.062
106. M. Wang, B. Song, Q. Wei, Y. Shi, Improved mechanical properties of AlSi7Mg/nano-SiCp composites fabricated by selective laser melting. J. Alloys Compd. **810**, 151926 (2019). https://doi.org/10.1016/j.jallcom.2019.151926
107. D. Gu, Y. Yang, L. Xi, J. Yang, M. Xia, Laser absorption behavior of randomly packed powder-bed during selective laser melting of SiC and TiB2 reinforced Al matrix composites. Opt. Laser Technol. **119**, 105600 (2019). https://doi.org/10.1016/j.optlastec.2019.105600
108. L.K. Ang, Y.Y. Lau, R.M. Gilgenbach, H.L. Spindler, Analysis of laser absorption on a rough metal surface. Appl. Phys. Lett. **70**, 696–698 (1997). https://doi.org/10.1063/1.118242
109. W.H. Yu, S.L. Sing, C.K. Chua, C.N. Kuo, X.L. Tian, Particle-reinforced metal matrix nanocomposites fabricated by selective laser melting: a state of the art review. Prog. Mater. Sci. **104**, 330–379 (2019). https://doi.org/10.1016/j.pmatsci.2019.04.006
110. F. Chang, D. Gu, D. Dai, P. Yuan, Selective laser melting of in-situ Al4SiC4+SiC hybrid reinforced Al matrix composites: influence of starting SiC particle size. Surf. Coat. Technol. **272**, 15–24 (2015). https://doi.org/10.1016/j.surfcoat.2015.04.029
111. Y.K. Xiao, Z.Y. Bian, Y. Wu, G. Ji, Y.Q. Li, M.J. Li, Q. Lian, Z. Chen, A. Addad, H.W. Wang, Effect of nano-TiB2 particles on the anisotropy in an AlSi10Mg alloy processed by selective laser melting. J. Alloys Compd. **798**, 644–655 (2019). https://doi.org/10.1016/j.jallcom.2019.05.279
112. Q. Tan, J. Zhang, Q. Sun, Z. Fan, G. Li, Y. Yin, Y. Liu, M.X. Zhang, Inoculation treatment of an additively manufactured

2024 aluminium alloy with titanium nanoparticles. Acta Mater. **196**, 1–16 (2020). https://doi.org/10.1016/j.actamat.2020.06.026

113. D. Gu, H. Wang, D. Dai, P. Yuan, W. Meiners, R. Poprawe, Rapid fabrication of Al-based bulk-form nanocomposites with novel reinforcement and enhanced performance by selective laser melting. Scr. Mater. **96**, 25–28 (2015). https://doi.org/10.1016/j.scriptamat.2014.10.011
114. D. Dai, D. Gu, M. Xia, C. Ma, H. Chen, T. Zhao, C. Hong, A. Gasser, R. Poprawe, Melt spreading behavior, microstructure evolution and wear resistance of selective laser melting additive manufactured AlN/AlSi10Mg nanocomposite. Surf. Coat. Technol. **349**, 279–288 (2018). https://doi.org/10.1016/j.surfcoat.2018.05.072
115. B. AlMangour, D. Grzesiak, J.-M. Yang, Selective laser melting of TiC reinforced 316L stainless steel matrix nanocomposites: influence of starting TiC particle size and volume content. Mater. Des. **104**, 141–151 (2016). https://doi.org/10.1016/j.matdes.2016.05.018
116. B. AlMangour, D. Grzesiak, J.M. Yang, In-situ formation of novel TiC-particle-reinforced 316L stainless steel bulk-form composites by selective laser melting. J. Alloys Compd. **706**, 409–418 (2017). https://doi.org/10.1016/j.jallcom.2017.01.149
117. D. Gu, J. Ma, H. Chen, K. Lin, L. Xi, Laser additive manufactured WC reinforced Fe-based composites with gradient reinforcement/matrix interface and enhanced performance. Compos. Struct. **192**, 387–396 (2018). https://doi.org/10.1016/j.compstruct.2018.03.008
118. B. AlMangour, Y.-K. Kim, D. Grzesiak, K.-A. Lee, Novel TiB2-reinforced 316L stainless steel nanocomposites with excellent room- and high-temperature yield strength developed by additive manufacturing. Compos. B Eng. **156**, 51–63 (2019). https://doi.org/10.1016/j.compositesb.2018.07.050
119. C.L. Wu, S. Zhang, C.H. Zhang, J.B. Zhang, Y. Liu, J. Chen, Effects of SiC content on phase evolution and corrosion behavior of SiC-reinforced 316L stainless steel matrix composites by laser melting deposition. Opt. Laser Technol. **115**, 134–139 (2019). https://doi.org/10.1016/j.optlastec.2019.02.029
120. E. Fereiduni, A. Ghasemi, M. Elbestawi, Selective laser melting of aluminum and titanium matrix composites: recent progress and potential applications in the aerospace industry. Aerospace **7**, 77 (2020). https://doi.org/10.3390/aerospace7060077
121. R. Wang, L. Xi, K. Ding, B. Gökce, S. Barcikowski, D. Gu, Powder preparation during ball milling and laser additive manufacturing of aluminum matrix nanocomposites: powder properties, processability and mechanical property. Adv. Powder Technol. **33**, 103687 (2022). https://doi.org/10.1016/j.apt.2022.103687
122. G. Xue, L. Ke, H. Zhu, H. Liao, J. Zhu, X. Zeng, Influence of processing parameters on selective laser melted SiCp/AlSi10Mg composites: densification, microstructure and mechanical properties. Mater. Sci. Eng. A (2019). https://doi.org/10.1016/j.msea.2019.138155
123. D. Dai, D. Gu, Influence of thermodynamics within molten pool on migration and distribution state of reinforcement during selective laser melting of AlN/AlSi10Mg composites. Int. J. Mach. Tools Manuf **100**, 14–24 (2016). https://doi.org/10.1016/j.ijmachtools.2015.10.004
124. Z. Hu, F. Chen, J. Xu, Q. Nian, D. Lin, C. Chen, X. Zhu, Y. Chen, M. Zhang, 3D printing graphene-aluminum nanocomposites. J. Alloys Compd. **746**, 269–276 (2018). https://doi.org/10.1016/j.jallcom.2018.02.272
125. Z. Zhao, P. Bai, R.D.K. Misra, M. Dong, R. Guan, Y. Li, J. Zhang, L. Tan, J. Gao, T. Ding, W. Du, Z. Guo, AlSi10Mg alloy nanocomposites reinforced with aluminum-coated graphene: selective laser melting, interfacial microstructure and property analysis. J. Alloys Compd. **792**, 203–214 (2019). https://doi.org/10.1016/j.jallcom.2019.04.007
126. D. Gu, X. Rao, D. Dai, C. Ma, L. Xi, K. Lin, Laser additive manufacturing of carbon nanotubes (CNTs) reinforced aluminum matrix nanocomposites: processing optimization, microstructure evolution and mechanical properties. Addit. Manuf. **29**, 100801 (2019). https://doi.org/10.1016/j.addma.2019.100801
127. L.Y. Jiang, T.T. Liu, C.D. Zhang, K. Zhang, M.C. Li, T. Ma, W.H. Liao, Preparation and mechanical properties of CNTs-AlSi10Mg composite fabricated via selective laser melting. Mater. Sci. Eng. A **734**, 171–177 (2018). https://doi.org/10.1016/j.msea.2018.07.092
128. S.D. Jadhav, S. Dadbakhsh, R. Chen, R. Shabadi, J.P. Kruth, J. Van Humbeeck, K. Vanmeensel, Modification of electrical and mechanical properties of selective laser-melted CuCr0.3 alloy using carbon nanoparticles. Adv. Eng. Mater. **22**, 1–14 (2020). https://doi.org/10.1002/adem.201900946
129. L.J. Jallo, M. Schoenitz, E.L. Dreizin, R.N. Dave, C.E. Johnson, The effect of surface modification of aluminum powder on its flowability, combustion and reactivity. Powder Technol. **204**, 63–70 (2010). https://doi.org/10.1016/j.powtec.2010.07.017
130. D. Bergström, J. Powell, A.F.H. Kaplan, A ray-tracing analysis of the absorption of light by smooth and rough metal surfaces. J. Appl. Phys. (2007). https://doi.org/10.1063/1.2738417
131. R. Wu, S. Liang, A. Pan, Z. Yuan, Y. Tang, X. Tan, D. Guan, Y. Yu, Fabrication of nano-structured super-hydrophobic film on aluminum by controllable immersing method. Appl. Surf. Sci. **258**, 5933–5937 (2012). https://doi.org/10.1016/j.apsusc.2011.10.029
132. Y. Huang, D.K. Sarkar, X. Grant Chen, Superhydrophobic aluminum alloy surfaces prepared by chemical etching process and their corrosion resistance properties. Appl. Surf. Sci. **356**, 1012–1024 (2015). https://doi.org/10.1016/j.apsusc.2015.08.166
133. H. Adelkhani, S. Nasoodi, A.H. Jafari, A study of the morphology and optical properties of electropolished aluminum in the Vis-IR region. Int. J. Electrochem. Sci. **4**, 238–246 (2009)
134. Y. Arata, I. Miyamoto, Some fundamental properties of high power laser beam as a heat source (Report 2). Trans. Jpn. Weld. Soc. **3**, 152–162 (1972)

135. S.D. Jadhav, J. Vleugels, J. Kruth, J. Van Humbeeck, K. Vanmeensel, Mechanical and electrical properties of selective laser-melted parts produced from surface-oxidized copper powder. Mater. Des. Process. Commun. **2**, 1–8 (2020). https://doi.org/10.1002/mdp2.94
136. S.D. Jadhav, P.P. Dhekne, S. Dadbakhsh, J.P. Kruth, J. Van Humbeeck, K. Vanmeensel, Surface modified copper alloy powder for reliable laser-based additive manufacturing. Addit. Manuf. **35**, 101418 (2020). https://doi.org/10.1016/j.addma.2020.101418
137. M. Nozar, V. Pokorna, I. Zetkova, Potential health hazards of additive manufacturing, in *Annals of DAAAM and Proceedings of the International DAAAM Symposium*, vol. 30. (2019), pp. 654–662. https://doi.org/10.2507/30th.daaam.proceedings.090
138. J. Walter, A. Baumgärtel, M. Hustedt, R. Hebisch, S. Kaierle, Inhalation exposure to hazardous substances during powder-bed processes. Procedia CIRP **74**, 295–299 (2018). https://doi.org/10.1016/j.procir.2018.08.114
139. Y. Huang, G.A. Risha, V. Yang, R.A. Yetter, Effect of particle size on combustion of aluminum particle dust in air. Combust. Flame **156**, 5–13 (2009). https://doi.org/10.1016/j.combustflame.2008.07.018
140. J. Cai, C. Li, P. Amyotte, W. Yuan, C. Yuan, G. Li, Effect of solid inertants and sample inclination angle on fire hazard of metallic powder layers. Process. Saf. Environ. Prot. **129**, 321–325 (2019). https://doi.org/10.1016/j.psep.2019.06.030
141. U. Masood Chaudry, K. Hamad, T. Abuhmed, Machine learning-aided design of aluminum alloys with high performance. Mater Today Commun. **26**, 101897 (2021). https://doi.org/10.1016/j.mtcomm.2020.101897
142. D.A. de Moura, G.L. de Gouveia, G. Figueira, A. Garcia, P. Gargarella, J.E. Spinelli, Laser remelting of AlSi10Mg(-Ni) alloy surfaces: influence of Ni content and cooling rate on the microstructure. Int. J. Adv. Manuf. Technol. **120**, 8117–8132 (2022). https://doi.org/10.1007/s00170-022-09263-4
143. J.S. Zuback, T.A. Palmer, T. DebRoy, Additive manufacturing of functionally graded transition joints between ferritic and austenitic alloys. J. Alloys Compd. **770**, 995–1003 (2019). https://doi.org/10.1016/j.jallcom.2018.08.197
144. D.L. de Mattos Nascimento, R. Mury Nepomuceno, R.G.G. Caiado, J.M. Maqueira, J. Moyano-Fuentes, J.A. Garza-Reyes, A sustainable circular 3D printing model for recycling metal scrap in the automotive industry. J. Manuf. Technol. Manag. **33**, 876–892 (2022). https://doi.org/10.1108/JMTM-10-2021-0391
145. J.F.T. de Souza, S.A. Pacca, Carbon reduction potential and costs through circular bioeconomy in the Brazilian steel industry. Resour. Conserv. Recycl. (2021). https://doi.org/10.1016/j.resconrec.2021.105517
146. A.P.M. de Araujo, C.S. Kiminami, V. Uhlenwinkel, P. Gargarella, Processability of recycled quasicrystalline Al-Fe-Cr-Ti composites by selective laser melting—a statistical approach. Materialia (Oxford) (2022). https://doi.org/10.1016/j.mtla.2022.101377
147. T. Delacroix, F. Lomello, F. Schuster, H. Maskrot, J.P. Garandet, Influence of powder recycling on 316L stainless steel feedstocks and printed parts in laser powder bed fusion. Addit. Manuf. (2022). https://doi.org/10.1016/j.addma.2021.102553
148. X. He, D. Kong, Y. Zhou, L. Wang, X. Ni, L. Zhang, W. Wu, R. Li, X. Li, C. Dong, Powder recycling effects on porosity development and mechanical properties of Hastelloy X alloy during laser powder bed fusion process. Addit. Manuf. (2022). https://doi.org/10.1016/j.addma.2022.102840